nature energy

Article

https://doi.org/10.1038/s41560-025-01836-3

Direct air capture of CO_2 in an electrochemical hybrid flow cell with a spatially isolated phenazine electrode

Received: 3 June 2024

Accepted: 10 July 2025

Published online: 22 August 2025

Check for updates

Xinyu Jin[1,5], Shijian Jin[2,5], Lu Li[3], Roy G. Gordon[2,4], Pan Wang[3] ✉, Michael J. Aziz[2] ✉ & Yunlong Ji[1] ✉

CO_2 capture based on a pH swing driven electrically through the reversible proton-coupled electron transfer of organic molecules could be powered entirely by clean electricity. A major technical challenge is the reversible chemical oxidation of the reduced organics by atmospheric O_2, which can lower energy efficiency and capture capacity. Here we report the development of a hybrid phenazine flow cell system that uses a pH-swing direct air capture (DAC) process, utilizing redox-active cyclic poly(phenazine sulfide) fabricated solid electrodes. The system maintains a separation between the air and the O_2-sensitive reduced phenazine, enabling stable and effective CO_2 capture from gas mixtures containing O_2. This flow cell demonstrated substantial oxygen compatibility, exhibiting a coulombic efficiency of 99% and requiring only 73 kJ mol^{-1} CO_2 for simulated flue gas and 104 kJ mol^{-1} CO_2 for DAC. The strategy of isolating vulnerable species offers an efficient pathway for DAC and may be broadly applicable to avoiding undesirable side reactions in other electrochemical devices.

Direct air capture (DAC), the process of capturing CO_2 directly from the atmosphere, is an area of rapidly growing activity for mitigating rising atmospheric CO_2 levels[1,2]. Several industrial attempts are underway, with companies such as Climeworks and Carbon Engineering already commercializing their DAC technologies[3]. Climeworks uses a solid amine absorbent within a thermal–pressure swing cycle to capture dilute CO_2. Carbon engineering utilizes a highly alkaline liquid to capture airborne CO_2, forming solid carbonate precipitates. The carbonates are subsequently calcined in an oxygen fired kiln to release pure CO_2 at 900 °C. While these approaches are relatively straightforward, a substantial challenge lies in the high thermal energy required for sorbent or solvent regeneration. This pushes the overall process energy consumption to a range of 308–440 kJ mol^{-1} CO_2, far exceeding the theoretical minimum of 19 kJ mol^{-1} CO_2 for DAC[4]. Beyond the high energy cost and capital expenditure associated with high-temperature processing, concerns remain regarding material degradation, volatility and process scalability.

Unlike traditional, heat-driven capture methods, electrochemically mediated CO_2 capture (EMCC) offers an environmentally friendly alternative[5]. EMCC operates at ambient temperatures and can be coupled with renewable energy sources, promoting a closed-loop carbon economy. Among various EMCC techniques being explored[6] are pH gradient manipulation[7,8], redox-active capture agents[9–11], electrochemically mediated amine regeneration[12] and an electrochemically induced pH swing[13,14]. One implementation of the latter method uses proton-coupled electron transfer (PCET) in a redox-active molecule to swing the pH of a sorbent solution, enabling it to absorb CO_2 at high pH and release it at lower pH. Recent advancements utilize PCET to achieve

[1]School of Chemistry and Materials Science, Hangzhou Institute for Advanced Study, University of Chinese Academy of Sciences, Hangzhou, China. [2]John A. Paulson School of Engineering and Applied Sciences, Harvard University, Cambridge, MA, USA. [3]Key Laboratory of Precise Synthesis of Functional Molecules of Zhejiang Province, Department of Chemistry, School of Science, Westlake University, Hangzhou, China. [4]Department of Chemistry and Chemical Biology, Harvard University, Cambridge, MA, USA. [5]These authors contributed equally: Xinyu Jin, Shijian Jin.
✉e-mail: wangpan@westlake.edu.cn; maziz@harvard.edu; jiyunlong@ucas.ac.cn

https://doi.org/10.1038/s41560-025-01836-3

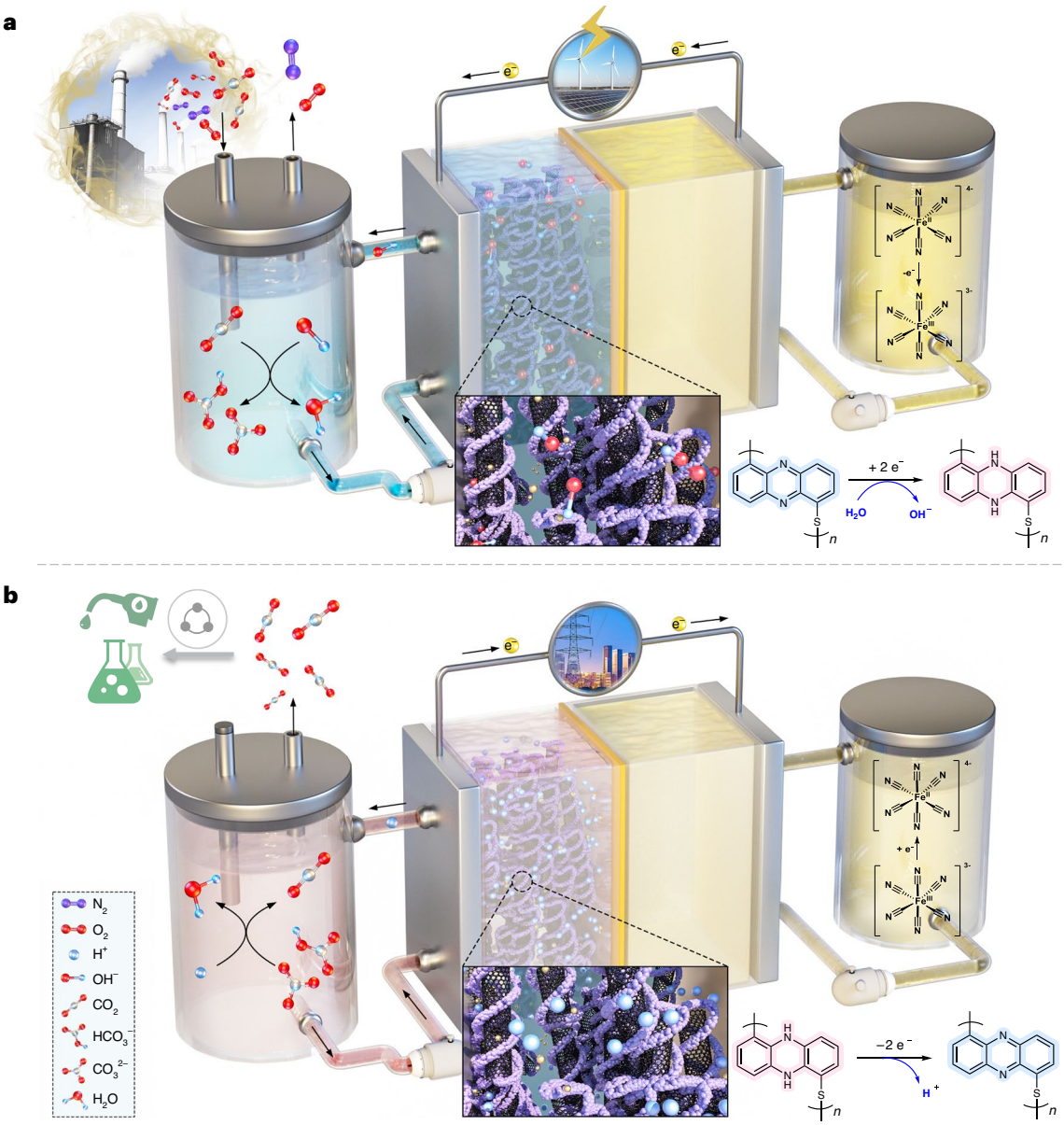

Fig. 1 | Schematic of the hybrid flow carbon capture set-up. The negative electrode, composed of carbon nanotubes loaded with phenazine macrocycles (CPS) for PCET reactions, is spatially isolated from the sorbent solution for CO_2 capture. **a**, CO_2 capture process. **b**, CO_2 release process.

this pH swing with organic molecules composed of Earth-abundant elements[4,15–20]. Notably, these PCET-active molecules not only exhibit low energy demands (30–130 kJ mol^{-1} CO_2 at 10–150 mA cm^{-2}) for CO_2 separation from point sources but also can demonstrate remarkable stability[4,15,16]. Their capacity fade rate can fall below 0.01% per day[16]. Such longevity could lead to a scalable capture system with an extended operational lifetime, which in turn leads to lower maintenance costs.

While pH-swing systems involving organic molecule electrochemistry exhibit promising attributes such as high current density, potentially leading to low capital costs, and low energy cost and long lifetime, their deployment faces major challenges in the presence of oxygen[15,16,19]. Oxygen reversibly oxidizes electrochemically reduced active species, leading to diminished energy efficiency (the reciprocal of work per mole of CO_2 captured) and compromised CO_2 capture capacity. This ultimately leads to cell imbalance, where all electroactive materials on both sides become fully oxidized, halting operation. Consequently, these systems are unsuitable for DAC owing to the significantly higher oxygen concentration compared with CO_2 in ambient air. Developing oxygen-resistant molecules for DAC presents a notable challenge. Molecules capable of inducing significant pH swings in water beyond pH 13 require high pK_a values >13 in their reduced form. Typically, high pK_a correlates with strong nucleophilicity and very negative reduction potentials, making these molecules highly susceptible to oxidation by molecular oxygen. While it is possible to engineer molecules with more positive reduction potentials, reducing reactivity towards oxygen, this compromises their proton affinity by lowering their pK_a in the reduced form, which in turn hinders pH-swing-based capture capacity[21,22].

Here, we report a hybrid flow/solid-electrode cell of a unique design that enables pH-swing carbon capture without direct exposure of the redox-active organic molecules to oxygen. In this developed EMCC system, rather than dissolving active substances in a solution, redox-active phenazine molecules are integrated into insoluble macrocycles that are subsequently fabricated into solid electrode materials (Fig. 1). During cell charging, a phenazine core in the electrode accepts two electrons while concurrently acquiring two protons from aqueous electrolyte. This process (Supplementary Note 1), described by

https://doi.org/10.1038/s41560-025-01836-3

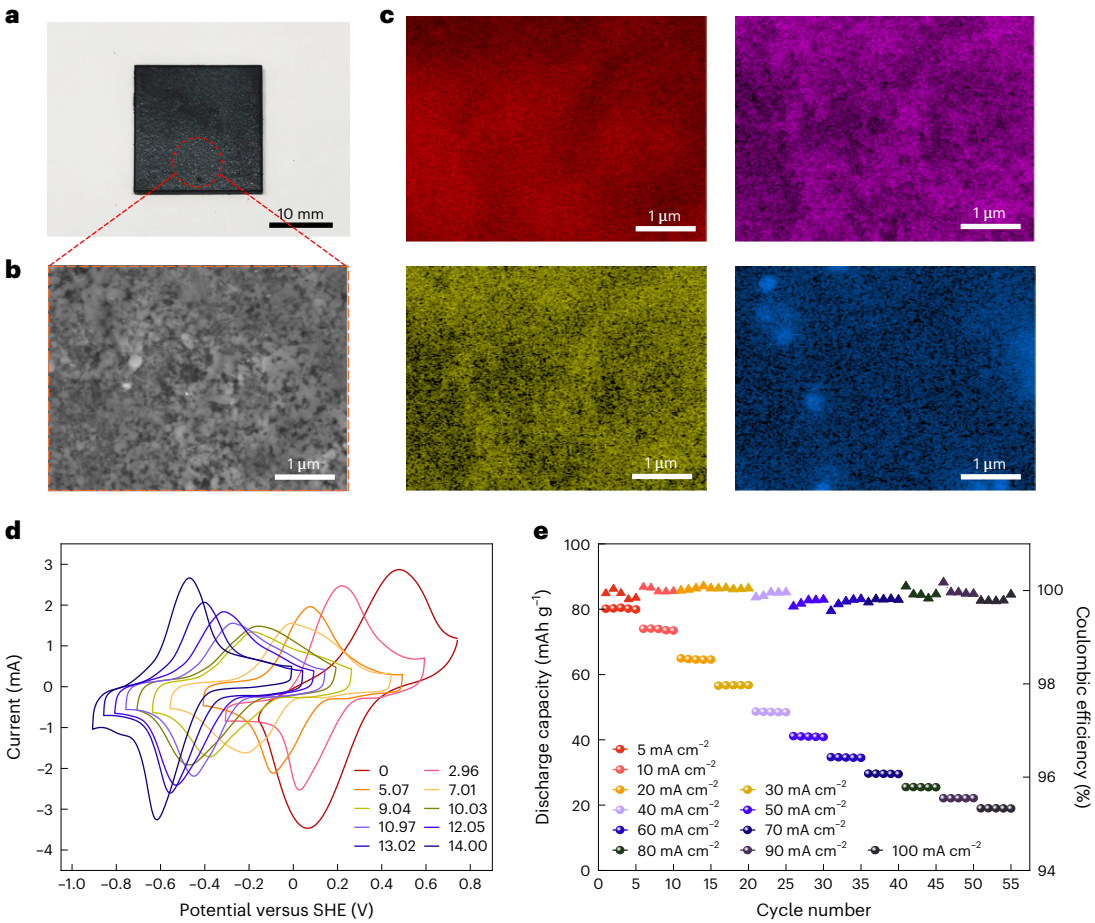

Fig. 2 | Characterization of the CPS-CNT electrode and rate performance of the CPS-CNT flow cell. a, A digital photo of the CPS-CNT electrode. Scale bar, 10 mm. **b**, A typical SEM image. Scale bar, 1 µm. The characterization area is highlighted by a red dotted circle in (**a**). **c**, Corresponding EDS elemental maps of C (red), N (pink), S (yellow) and F (blue) in the CPS-CNT electrode. Scale bar, 1 µm. The imaging area is shown in (**b**). **d**, CVs of dropcast CPS-CNT electrodes in buffered solutions in 1.0 M KCl at different pH. An Ag/AgCl reference electrode filled with 3.0 M KCl salt bridge solution was used for the CV test. Potentials are referenced to the standard hydrogen electrode (SHE). **e**, Discharge capacity and Coulombic efficiency of CPS-CNT flow cell in 1.0 M KCl at different current densities. Five cycles were performed for each current density.

previous literature as deacidification (equation (1) in Supplementary Note 1), results in the release of two hydroxide ions into the electrolyte. The resultant highly alkaline solution is then transported to a separate reservoir for subsequent CO_2 capture, designated as the absorption step (equation (2) in Supplementary Note 1). The spatial separation between the CO_2 source and the oxygen-sensitive phenazine allows the system to operate effectively in the presence of O_2, which is found in almost all CO_2 sources such as flue gas and air. The electrolyte, upon saturation with dissolved inorganic carbon (DIC), is pumped back to the electrode compartment for electrochemical acidification (equation (3) in Supplementary Note 1). This process generates protons, leading to simultaneous desorption (equation (4) in Supplementary Note 1) of pure CO_2 from the solution. The hybrid phenazine flow cell here demonstrates a low CO_2 molar work of 73 kJ mol^{-1} CO_2 for simulated flue gas and 104 kJ mol^{-1} CO_2 for DAC, respectively. The system operates with a high coulombic efficiency of ~99%, suggesting a distinct advantage in terms of oxygen compatibility. This particular design offers an alternative path towards DAC compared with the difficult task of breaking the CO_2 affinity and oxygen susceptibility trade-off through molecular engineering.

Synthesis and characterization of CPS

Phenazine, a prototypical structure centre for PCET reactions, was used as the reaction core to synthesize a cyclic phenazine macrocycle with sulfur as the linker (Supplementary Note 2). Analysis of the macrocycle by matrix-assisted laser desorption/ionization time-of-flight (MALDI-TOF) mass spectrometry revealed that no end bromine groups existed. This was indicated by the linear plot between the mass-to-charge m/z values and the number of repeating units with an intercept value of 0, which corroborates the formation of cyclic structure in the synthesized cyclic poly(phenazine sulfide) (CPS) (Supplementary Fig. 1). Fourier-transform infrared spectroscopy measurements further confirmed the complete conversion of the monomer to CPS, as indicated by the disappearance of the C(Ar)–Br vibrational absorption peak at 600–700 cm^{-1} and the emergence of a new peak at 1,454 cm^{-1}, corresponding to C(Ar)–S bond formation (Supplementary Fig. 2). Powder X-ray diffraction and high-resolution transmission electron microscopy analyses suggest that CPS exhibits a semi-crystalline structure, characterized by predominantly amorphous regions with localized crystalline domains (Supplementary Figs. 3 and 4).

The CPS-carbon nanotube (CNT) electrode shown in Fig. 2a,b is prepared by blending CPS macrocycle with multiwalled carbon nanotubes (MWCNTs) in ethanol, using polyvinylidene fluoride (PVDF) as a binder (Supplementary Note 3). The hollow MWCNT not only provide a high conductivity of the electrode but also enhance the contact surface area between macrocycles and electrolytes, enabling improved ionic diffusion and high utilization. The mixture undergoes thorough grinding, resulting in a reduction in particle size and ensuring

uniform and complete contact between CPS and MWCNT. After drying in a vacuum overnight to remove the residual solvent, the mixture was pressed with a pressure of 10 MPa to obtain a sheet-like electrode with an area of 2 × 2 cm^2 whose thickness depends on the material loading. The CPS-CNT electrode, incorporating 47% macrocycle, possesses a theoretical capacity of 120.0 mAh g^{-1}. As shown with scanning electron microscopy (SEM), compared with the individual macrocycle or MWCNT, the CPS-CNT electrode shows the macrocycle particles stacked together, interspersed with linear nanotubes (Supplementary Figs. 5–7). To further identify the electronic structure of the CPS-CNT electrode, X-ray photoelectron spectroscopy (XPS) was performed to analyse the element composition and distribution (Supplementary Fig. 8). The XPS spectra of the electrode show the peaks of C 1*s*, N 1*s*, S 2*s* and S 2*p* located at 285, 399, 228 and 164 eV, respectively. The F 1*s* peak observed at 688 eV was attributed to the presence of the PVDF binder, while the O 1*s* peak at 532 eV originated from atmospheric oxygen. Energy-dispersive X-ray spectroscopy (EDS) elemental maps (Fig. 2c and Supplementary Fig. 9) revealed a uniform distribution of carbon (C), nitrogen (N) and sulfur (S), while the aggregation of fluorine (F) may be attributed to a small amount of accumulated PVDF binder.

Similar to dissolved phenazine moieties, the reduced form of CPS exhibits a high pK_a (>14), as indicated by cyclic voltammetry (CV) data (Fig. 2d) and the characteristic −0.059 V pH^{-1} slope observed in the Pourbaix diagram (Supplementary Fig. 10) across the entire pH range (0–14). This translates to efficient PCET throughout the operation, ideally for CO_2 capture and release. CV tests performed under a CO_2 atmosphere in a 0.4 M K_2CO_3 and 0.1 M $KHCO_3$ solution revealed reversible redox activity (Supplementary Fig. 11), validating the electrode's compatibility with both gaseous CO_2 and DIC species. To confirm electrochemical stability, control experiments were performed using a background electrode (MWCNT + PVDF), an oxidized CPS-CNT electrode (pristine state) and a reduced CPS-CNT electrode. All electrodes were immersed in 1.0 M KCl, and the soaking solutions were monitored via ultraviolet–visible (UV–vis) spectroscopy for 30 days. No dissolution of CPS was detected, confirming negligible leaching under electrochemical conditions (Supplementary Fig. 12). The CPS-CNT electrode demonstrates effective water contact, with contact angles of 49.47° for CPS and 64.32° for the CPS-CNT electrode (prepared with PVDF binder) (Supplementary Fig. 13). Brunauer–Emmett–Teller analysis under CO_2 and N_2 atmospheres revealed that CPS powder exhibits a predominant pore size of 5.3 Å in the microporous region, with minimal pore size distribution above 1 nm (Supplementary Figs. 14 and 15). This porous structure facilitates water penetration, ensuring efficient contact between the CPS-CNT electrode and water.

CO_2 capture cells and the energetic cost evaluation

A hybrid flow battery was assembled with a cation exchange membrane Nafion NC700 (Supplementary Note 4). As with previously established flow battery works[23], the positive electrolyte (posolyte) leverages $K_3Fe(CN)_6$/$K_4Fe(CN)_6$ owing to their high stability and solubility. The key innovation of the system lies in the unique negative electrode composition: a CPS-CNT electrode that is immersed, rather than dissolved, in a 1 M KCl electrolyte. The rate performance of the flow cell is illustrated in Fig. 2e and Supplementary Fig. 16, where various current densities were applied during the charge and discharge cycles of the cell within the voltage cut-off of 1.5 V to 0.0 V. The cell at 10 mA cm^{-2} accessed a capacity of 74 mAh g^{-1}. With increasing current density, there was a decline in capacity and energy efficiency at the same cut-off voltage due to the increased ohmic loss. The coulombic efficiency remained above 99% for all rate tests. The pH of the electrolyte after battery charging was measured, demonstrating a Faradaic efficiency exceeding 99% (Supplementary Fig. 17). Both coulombic efficiency and Faradaic efficiency values close to 100% demonstrate the reversibility of the battery cycling and negligible side reactions. The cell with an open-circuit voltage (OCV) of ~1.0 V exhibited a stable cycle performance and delivered a peak power density of approximately 85 mW cm^{-2}, indicating it also functions as an energy storage device that could significantly improve the system economics[16].

The energetic cost associated with flue gas capture or DAC was evaluated in the hybrid flow system (Fig. 3 and Supplementary Note 5). Figure 3b–f illustrates an electrochemical carbon capture cycle using the hybrid flow system. Within this cycle, pure CO_2 was extracted from a synthetic flue gas blend comprising 20% CO_2, 20% O_2 and 60% N_2. The cell was charged galvanostatically at 10 mA cm^{-2}, followed by a potentiostatic hold at a voltage limit of 1.4 V. The CPS electrode underwent reduction and the deacidification step commenced until t = 1.0 h. Through PCET, the pH of the negative electrolyte (negolyte), recirculated between the CPS-CNT electrode and reservoir via a peristaltic pump, increased above 13. Meanwhile, both upstream mass flow controllers (MFCs) remained closed, as indicated by the absence of downstream CO_2 partial pressure (pCO_2) or gas flow in Fig. 3e,f. Upon the completion of deacidification, the entire negolyte was transferred to the reservoir by changing the flow direction of the liquid, and liquid valves on the pump tubing (indicated in Fig. 3a) were closed to isolate the electrodes from the reservoir environment. Subsequently, the flue gas MFC was open, enabling flue gas influx into the negolyte reservoir at 5 ml min^{-1}. The initially low gas flow rate (<5 ml min^{-1}; Fig. 3f) and pCO_2 (<0.2 bar; Fig. 3e) are attributed to CO_2 absorption by the alkalinized negolyte. Consequently, pH gradually decreased, levelling off to pH ~7 at t = 3.0 h, signalling an equilibrium between negolyte and headspace gas, denoting the completion of the CO_2 absorption step. At t = 3.6 h, the flue gas MFC was closed and the pure CO_2 stream was delivered. The liquid valves on the pump tubing were opened and the electrolyte circulation between cell and reservoir was restarted at t = 4.5 h, exhibiting a dip in pCO_2 (Fig. 3e) and gas flow rate (Fig. 3f), resulting from additional CO_2 absorption when residual alkaline solution-containing electrode contacted recirculated electrolyte and headspace CO_2. The acidification and CO_2 outgassing commenced in a pure CO_2 (1 bar) environment at t = 5.3 h. As total alkalinity (TA)[4] was consumed by the oxidation of reduced CPS, CO_2 outgassing was recorded by the downstream flow meter as >5 ml min^{-1} net gas flow. The downstream gas flow rate dropped to 5 ml min^{-1} baseline at t = 6.5 h, indicating that all CO_2 release was completed. Throughout the entire cycling process, the pH of the positive electrode exhibited negligible changes (Supplementary Fig. 18).

The profiles of five cycles reflecting the continuous CO_2 capture and release processes exhibited high reproducibility (Supplementary Figs. 19 and 20 and Supplementary Table 1), suggesting good system stability. Leveraging the innovative design of the hybrid flow system and the cycling protocol for distinct deacidification and capture phases, the system is invulnerable to oxygen. Across the five cycles, the coulombic efficiency was 98.9 ± 0.1%, demonstrating the high resistance against oxygen. The error bars represent the standard deviation of five cycles. The average molar work for CO_2 stood at 73.4 ± 3.5 kJ mol^{-1} CO_2, with a detailed calculation method outlined in Supplementary Note 6. By contrast, in one capture cycle where the gas mixture containing 20% CO_2, 20% O_2 and 60% N_2 was continuously fed during the entire deacidification and capture step (Supplementary Fig. 21), the coulombic efficiency decreased to 69%, and the CO_2 molar work increased to 110 kJ mol^{-1} CO_2. These results demonstrate the necessity of our spatial separation strategy to protect oxygen-sensitive PCET reagents from oxidation.

Next, we demonstrated a DAC process utilizing the hybrid flow cell. Figure 3g–k depicts a representative cycle wherein CO_2 is extracted from ambient air (CO_2 concentration ~400 ppm). The cycling protocol closely resembled the previous flue gas capture cycle, except for the switch to air as the upstream gas source infused into the negolyte solution at 1 l min^{-1}. As the elevated flow rate surpassed the flow meter's measurement limit, it was not reflected in Fig. 3k. Similarly, the slight change in air pCO_2 was too insignificant to appear on the CO_2 sensor in Fig. 3j. The endpoint of absorption was determined by

https://doi.org/10.1038/s41560-025-01836-3

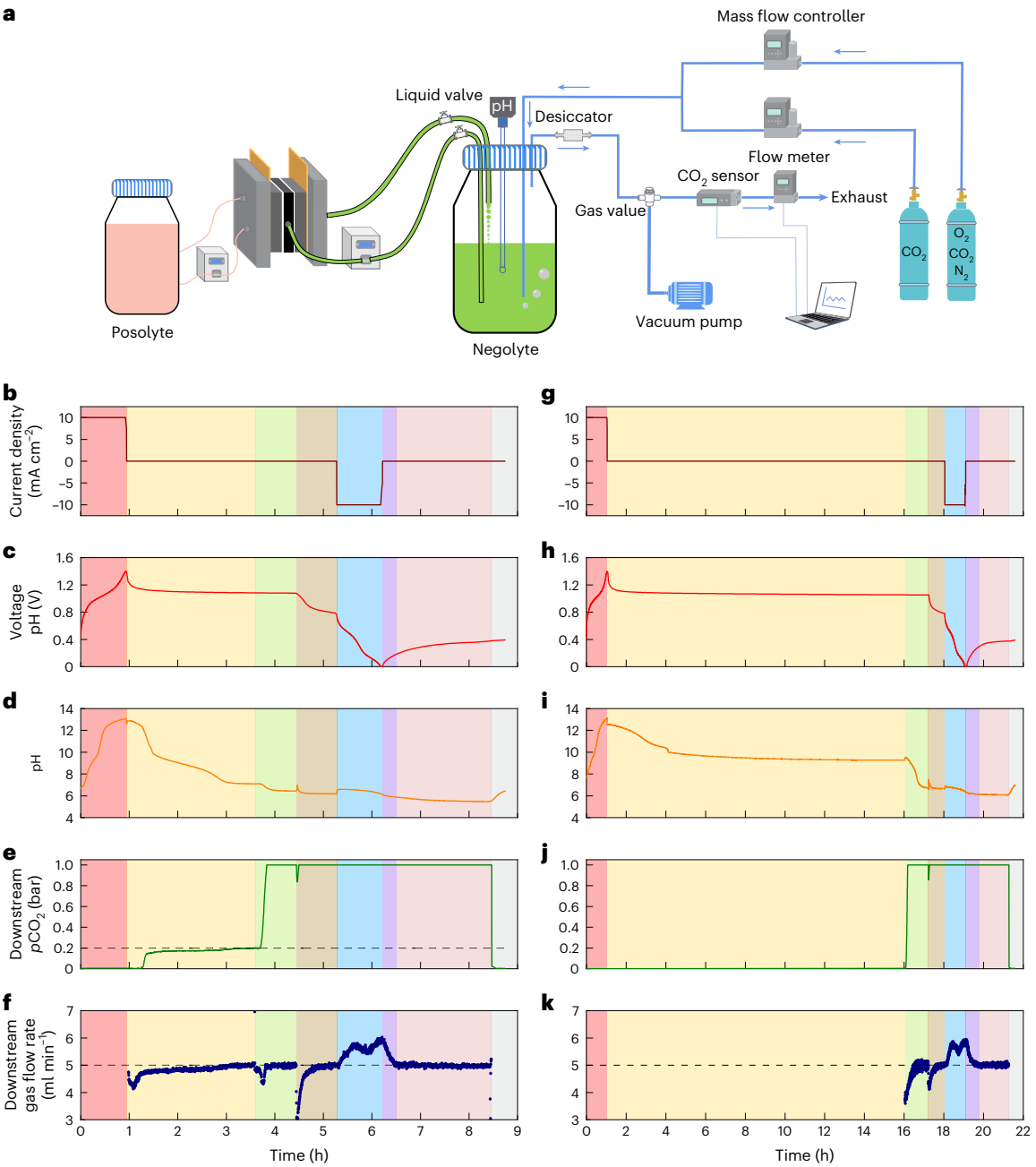

Fig. 3 | Schematic of the CO_2 capture–release system and two typical CO_2-concentrating cycles. a, Optimized scheme of CPS-CNT flow cell (Supplementary Note 4) for CO_2 capture–release experiments in the presence of O_2. The blue arrows indicate gas flow. **b**–**f**, A CO_2-concentrating cycle from 20% CO_2, 20% O_2 and 60% N_2 with the CPS-CNT flow cell. The feed gas was 20% CO_2, 20% O_2 and 60% N_2 for the capture step and was switched to pure CO_2 for the sweep step. The gas flow rate was set to 5 ml min^{-1}. **g**–**k**, A CO_2-concentrating cycle from air (laboratory air with fresh ventilation) with the CPS-CNT flow cell. The feed gas was air at a 1 l min^{-1} flow rate for the capture step (15 h) and was switched to pure CO_2 at 5 ml min^{-1} for the sweep step. Current density (**b**,**g**), voltage (**c**,**h**), pH of the negolyte (**d**,**i**), downstream CO_2 partial pressure (**e**,**j**; the dashed black baseline indicates pCO_2 = 0.2 bar) and downstream total gas flow rate (**f**,**k**; the dashed black baseline indicates 5 ml min^{-1}) are shown. The specific steps of the operation (Supplementary Note 5) are highlighted with each section in distinct colours in (**b**–**k**). Red, charge and deacidification process without feed gas; yellow, CO_2 capture process after spatially isolating the electrode from the absorbent solution; green, switch of the feed gas to pure CO_2 after absorption; brown, flow of the absorbent solution into the cell to contact the electrode; blue, discharge process and CO_2 release process; purple, continued CO_2 release process; pink, rest. Grey: removal of CO_2 gas from the system using a vacuum pump.

the stabilization of pH at a plateau of 9 (t = 16.0 h). In multicycle loops lasting over 110 h, the coulombic efficiency was 99.4 ± 0.1%, affirming the system's compatibility with oxygen and the average molar work for CO_2 was 104.3 ± 3.8 kJ mol^{-1} CO_2 (Supplementary Figs. 22 and 23 and Supplementary Table 1). In the conducted experiments, approximately 0.24 M of ΔTA was generated and subsequently consumed within a cycle for both flue gas and air capture. This resulted in alterations of about 0.23 M and 0.17 M in ΔDIC during the capture cycles of flue gas and air, respectively. The electrical work at a given ΔTA remained nearly identical for both flue gas and air capture, being 0.10 kJ for 0.24 M ΔTA, indicating that the disparity in ΔDIC was the primary determinant of the elevated molar cycle work. The reduced CO_2 partial pressure in

https://doi.org/10.1038/s41560-025-01836-3

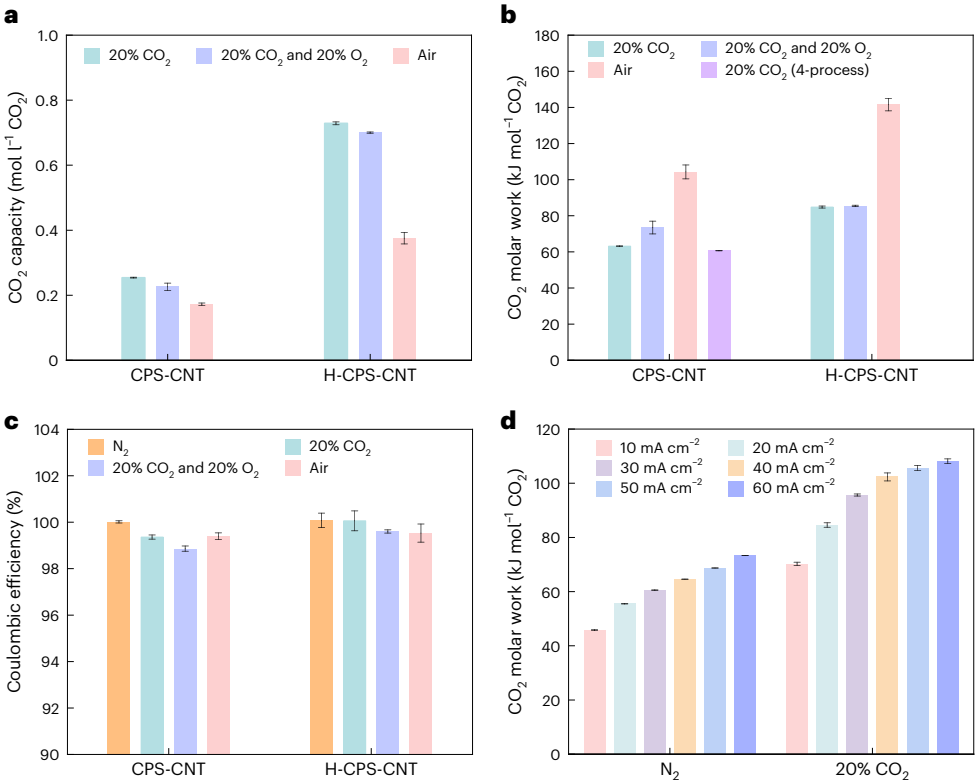

Fig. 4 | CO_2 capture performance at different conditions. a, CO_2 capture capacity at different charge capacities and feed gas at 10 mA cm^{-2}. **b**, CO_2 molar work under different feed gas and operating procedures at 10 mA cm^{-2}. **c**, Coulombic efficiency at different capacities and feed gas at 10 mA cm^{-2}. **d**, CO_2 molar work at different current densities. Left: CPS-CNT flow cell was cycled in a pure N_2 atmosphere. Right: CPS-CNT flow cell was cycled in a 20% CO_2, 80% N_2 atmosphere in the whole process. The error bars represent the standard deviation (s.d.) calculated over five cycles under each condition ($n = 5$), except for the DAC of the H-CPS-CNT cell, which was based on six cycles ($n = 6$). Data are presented as arithmetic mean values ± s.d.

the headspace led to a lower amount of conversion of gaseous CO_2 to DIC[4]. Furthermore, the low partial pressure of CO_2 in air decelerated kinetics by orders of magnitude[24]. Despite efforts to mitigate sluggish rates through increased upstream gas flow rates and prolonged contact durations, the gradual pH drift observed at $t = 16.0$ h suggested that additional CO_2 could have been captured. Clearly, implementing more effective contact methods can reduce the molar work of DAC by enhancing the rate and, consequently, the quantity of CO_2 captured within a set capture duration[25].

Furthermore, the CPS-CNT electrodes exhibited no detectable structural or chemical changes after direct CO_2 capture from ambient air, as demonstrated through comprehensive characterizations, including morphology analysis with SEM, elemental distribution analysis using EDS mapping, surface chemical analysis with XPS, pore structure analysis with both CO_2 and N_2 Brunauer–Emmett–Teller analysis, and resistance analysis with Nyquist impedance spectra (Supplementary Figs. 24–29). The UV–vis spectra of the electrolyte remained nearly identical before and after cycling (Supplementary Fig. 30). Future efforts should incorporate in situ spectroscopic analysis to monitor real-time structural and understand chemical changes in the electrodes during cycling.

CO_2 capture performance at different conditions

In addition, DAC experiments were conducted under current densities ranging from 10 to 60 mA cm^{-2} (Supplementary Figs. 31 and 32), demonstrating that the system remains operational even at a high current density of 60 mA cm^{-2}, ranking among the highest current densities reported for PCET-based capture systems (Supplementary Table 2). During the CO_2 desorption phase, pure CO_2 was used as a carrier gas to facilitate precise quantification of the released CO_2 volume through the integration of flow meters and CO_2 sensors. Experiments involving vacuum-based CO_2 release (Supplementary Figs. 33 and 34) were also conducted to demonstrate the reliability of our methods of evaluating the quantity of CO_2 captured and released.

Subsequently, we augmented the loading of CPS on the electrode (H-CPS-CNT, theoretical capacity 204 mAh g^{-1}; Supplementary Note 4 and Supplementary Figs. 35–38), leading to a threefold increase in ΔTA to ~0.72 M. Consequently, this enhancement in ΔTA corresponded to a threefold augmentation in CO_2 capacity in the electrolyte, yielding approximately 0.70 M and 0.38 M ΔDIC for flue gas and air capture, respectively. Despite the increased capacity leading to prolonged cycle times and extended exposure to oxygen, the coulombic efficiency remains above 99% (Supplementary Figs. 35–38). Notably, the multicycle experiments demonstrated excellent reproducibility between cycles (Supplementary Figs. 37 and 38), involving long-duration operation of more than 180 h. These extended cycling results highlight the stability and reliability of the capture cell for sustained carbon capture applications. The molar cycle work associated with the higher-capacity scenario surpassed that of the lower-capacity scenario, measuring at 85.4 ± 0.3 kJ mol^{-1} CO_2 and 141.5 ± 3.4 kJ mol^{-1} CO2 for flue gas (Supplementary Figs. 35 and 36) and air capture (Supplementary Figs. 37 and 38), respectively. Within electrodes of approximately equal size, in comparison with the CPS-CNT electrode, the H-CPS-CNT electrode incorporates a greater amount of active materials and a lesser quantity of conductive materials. This configuration endows it with a higher volumetric capacity; nevertheless, it concurrently gives rise to elevated ohmic losses (Supplementary Fig. 39), thereby culminating in a more substantial energy expenditure.

Note that, while differences in pCO_2 levels have a marked effect on molar cycle work, variations in O_2 partial pressure show minimal impact, as demonstrated in Fig. 4a–c and Supplementary Figs. 40–45. In Fig. 4a, the ΔDIC values remain nearly identical between scenarios with and without 20% O_2 under both low- and high-capacity conditions.

The coulombic efficiencies are ~99% despite O_2 concentrations (Fig. 4c), suggesting good oxygen compatibility. Owing to the isolation of the electroactive material from the electrolyte, prolonged exposure of the electrolyte to oxygen does not lead to further oxidation of the electroactive material. This isolation confers a notable advantage compared with full-flow systems, where electroactive materials are dissolved and cannot be separated, rendering them susceptible to oxygen-induced side reactions.

We also explored the varying current densities ranging from 10 to 60 mA cm^{-2} in either pure N_2 or 20% CO_2 + 80% N_2 in a galvanostatic cycling protocol (Supplementary Figs. 46 and 47). When 20% CO_2 was present in the atmosphere during the capture step, the CO_2 molar work varied between 70 and 108 kJ mol^{-1} CO_2 (Fig. 4d). For comparison, to provide a sense of the energy dissipated by the cell itself in the absence of CO_2, the CO_2 molar work, computed by dividing the cycle work in pure N_2 by the theoretical ΔDIC under 20% CO_2 conditions at the corresponding cell capacity and current density, ranged from 46 to 73 kJ mol^{-1} CO_2, as shown on the left side of Fig. 4d. The elevated CO_2 molar cost observed with the 20% CO_2 case can be attributed to a lower pH during the acidification step, leading to reduced energy return[15]. Higher current densities led to decreased CO_2 capture capacity and reduced process cycle duration at the same cut-off voltage. Because the absorption–release duration decreases proportionally with capacity, the average throughput remains nearly unchanged across tested current densities. These durations are expected to decrease with improved engineering of the gas–liquid contactor[25]. Elevated cycle work was observed at higher current densities due to heightened ohmic, electron-transfer and mass-transport overpotentials at higher densities[26] (Supplementary Fig. 48).

To gain deeper insights into these phenomena, we conducted high-frequency electrochemical impedance spectroscopy and polarization experiments across a state-of-charge (SOC) range of 10–100% (Supplementary Fig. 16b). The results aimed to delineate the individual contributions of different factors to the total resistance. The ohmic resistance, as determined by high-frequency electrochemical impedance spectroscopy, remained nearly constant throughout the SOC range at 1.5 Ω cm^2 (Supplementary Fig. 29). By contrast, polarization experiments indicated an overall area-specific resistance of approximately 3 Ω cm^2. This suggests that kinetics and mass-transport overpotentials collectively contribute 50% of the total overpotential, whereas the other 50% is attributed to ohmic overpotential, primarily stemming from membrane resistance and limited electrode conductivity. The current system's energy consumption (73 kJ mol^{-1} CO_2) for simulated flue gas with 20% O_2 is even close to that of the sodium 3,3′-(phenazine-2,3-diylbis(oxy))bis(propane-1-sulfonate) (DSPZ)[20] system (61 kJ mol^{-1} CO_2) without O_2 (Supplementary Table 2). Further optimizations on membrane design[27], molecular engineering[28], electrode composition[29] and flow pattern[30] can help to increase the capture capacity and lower the energetic cost. Engineering optimizations of the battery architecture, such as stacked cell designs[31], can further enhance the system's capture capacity. Key challenges such as electrode stack sealing and electrolyte circulation uniformity must be further optimized during future scaling-up efforts to ensure industrial viability.

Thermodynamics analysis of CO_2 capture cycles

Finally, we discuss the thermodynamics of CO_2 separation cycles using both hybrid and full flow systems, comparing their characteristics and discussing the implications of these distinct cycle methods. In our previous exploration of the full flow system[15], we identified a CO_2 separation cycle comprising four processes (Supplementary Fig. 49): deacidification with simultaneous CO_2 absorption (state 3′ → state 1), switching gas composition from low (0.1–0.5 bar) to high pCO_2 (1 bar) (state 1 → 1′), acidification with simultaneous CO_2 outgassing (state 1′ → 3), and switching gas composition from high to low pCO_2 (state 3 → 3′). The ideal cycle work for this set-up (concentrating 0.2 bar pCO_2 to 1 bar) is 5 kJ mol^{-1} CO_2 (ref. 4). By contrast, the hybrid flow system we examined in this study maintains the same processes but divides the concurrent deacidification and CO_2 absorption into two distinct steps (Supplementary Figs. 50 and 51): deacidification (state 3′ → state 4) and CO_2 absorption (state 4 → state 1). The ideal cycle work for this five-process cycle is 45 kJ mol^{-1} CO_2, significantly higher than the four-process cycle where deacidification and CO_2 absorption start simultaneously. This is because, during deacidification, the solution lacks buffering by DIC, as present in the four-process cycle, and there is an increased pH difference between deacidification and acidification (Supplementary Figs. 49c and 50c). However, our experiments revealed that the actual CO_2 molar cycle work for the four-process cycle (Fig. 4b and Supplementary Fig. 44) using the hybrid flow system was nearly identical to that of our typical five-process cycle (60.6 versus 63.2 kJ mol^{-1} CO_2). This discrepancy between theory and experiments arose because the solution during deacidification in the four-process cycle was not in equilibrium with the 0.2 bar CO_2 in the headspace, due to slower absorption kinetics, leading to higher-than-expected pH levels. In fact, the average pH during deacidification in the four-process and five-process cycles are very similar——7.43 and 7.49, respectively. This comparison underscores that transitioning from a four-process to a five-process cycle does not impact the experimental molar cycle work appreciably. The variance in experimental molar cycle work between the full and hybrid flow systems can be attributed to differences in ohmic, kinetic and mass transport overpotentials, as previously discussed.

Conclusions

In this work, an electrochemical CO_2 capture system based on a hybrid phenazine flow cell is developed, demonstrating low energetic cost and high O_2 compatibility. Unlike traditional systems where redox-active materials are dissolved in solution, here, CPS is integrated directly into the solid electrode materials and not exposed to electrolytes during the capture step. This configuration expands the application range of the pH-swing process driven by the PCET reactions of organic molecules, enabling their use for CO_2 capture in the presence of O_2 or other possible aggressive gases. This hybrid system operates at high coulombic efficiencies exceeding 99% and exhibits an energetic cost of 73 kJ mol^{-1} CO_2 for simulated flue gas and 104 kJ mol^{-1} CO_2 for DAC. It is expected that the hybrid cell design strategy of isolating vulnerable species could be broadly applicable to avoiding undesirable side reactions in other electrochemical devices.

Methods

Materials and methods

All solvents and reagents were commercially sourced and utilized without further purification unless otherwise stated. Detailed specifications are provided as follows: 1-bromo-2-nitrobenzene (98%), 2-bromoaniline (98%), potassium *tert*-butoxide (98%), *N*,*O*-bis(trimethylsilyl)acetamide (95%) and anhydrous sodium sulfide (Na_2S, 90%) were all purchased from Energy Chemical. *N*-methyl-2-pyrrolidone (99.5%, extra dry) was purchased from Shanghai Adamas Chemical. Acetonitrile (CH_3CN, 99.9%, extra dry) and tetrahydrofuran (99.9%, extra dry) were obtained from Sinopharm Chemical Reagent. Unless otherwise specified, all air-sensitive reactions were conducted under standard Schlenk techniques or in a nitrogen-filled glovebox, with all glassware oven-dried before use.

MALDI-TOF mass spectroscopy was conducted on the Shimadzu AXIMA-Performance in positive ion and linear mode. The oligomer sample was mixed with *trans*-2-[3-(4-tert-butylphenyl)-2-methyl-2-propenylidene]malononitrile matrix on a 384-well MALDI plate (Shimadzu) and dried at room temperature before testing. SEM and EDS analyses were carried out using a Zeiss Gemini 450. The XPS data were collected on a Thermo Fisher Scientific Nexsa G2 spectrometer, referenced to the C 1*s* peak at 284.8 eV. Fourier-transform infrared spectrometry measurements were conducted on a Thermo Fisher

Nicolet iS50 spectrometer using diamond attenuated total reflection technology, and the instrument recorded spectral information in reciprocal centimetres (cm^{-1}). UV–vis spectra were recorded on an Agilent Cary 60 spectrophotometer under ambient conditions. Powder X-ray diffraction patterns were collected on a Bruker D8 Advance diffractometer with Cu Kα radiation. The high-resolution transmission electron microscopy images were acquired using a Thermo Scientific Talos F200X G2 field emission high-resolution transmission electron microscope. The contact angle on the electrode surface was measured using an Attension Theta Flow instrument (Biolin Scientific) with deionized water as the probe liquid. Low-pressure gas physical adsorption–desorption was measured by a Micromeritics 3Flex surface area analyser with N_2 isotherms at 77 K and CO_2 isotherms at 273 K. All the materials were outgassed for 12 h under vacuum at 80 °C before measurement.

Synthesis of CPS

To a 150-ml high-pressure flask, 1,6-dibromophenazine (6.76 g, 20 mmol) and anhydrous sodium sulfide (Na_2S, 1.73 g, 20 mmol) were added into 50 ml of 1-methyl-2-pyrrolidone. The flask was sealed, and the mixture was heated to 205 °C with continuous stirring for 12 h under a nitrogen atmosphere. After cooling to room temperature, 500 ml of methanol was added to the reaction solution. The product was collected by filtration, washed with methanol and warm water three times, and then dried under vacuum at 60 °C for 24 h to afford a dark-green solid in 95% isolated yield.

Electrode preparation

Preparation of the working electrode for the CV test. To prepare the ink, 8.0 mg CPS and 8.0 mg MWCNT (LG Chem) were dispersed in a mixture of 100 µl Nafion D-520 solution (5 wt%) and 900 µl isopropanol. The mixture was sonicated for 30 min to form ink solution. The prepared ink was drop-cast onto a glassy carbon electrode with a mass loading of 0.1 mg mm^{-2} (area 7 mm^2) and air-dried for 1 h. CV measurements were conducted in a three-electrode system with 20 mV s^{-1} scan rate in various electrolytes, comprising a 3-mm glassy carbon working electrode, a Pt mesh counter electrode and a Ag/AgCl reference electrode (filled with 3.0 M KCl solution).

Preparation of CPS-CNT electrode as negative electrode for the hybrid flow cell. The electrode was prepared by mixing 0.32 g CPS, 0.32 g MWCNT and 0.04 g PVDF (Arkema) binder (8:8:1 by weight, respectively). The mixture was ground in a mortar for 1 h in ethanol to homogenize the particle size and enhance the contact between CPS and MWCNT. After solvent removal by vacuum drying at 60 °C overnight, the resulting powder was placed in a tablet press and pressed with a pressure of 10 MPa to obtain a sheet-like electrode with an area of 2 × 2 cm^2 and a thickness of 1.7 mm, denoted as the CPS-CNT electrode.

Following similar procedures described above, a high-capacity CPS-CNT electrode was prepared by controlling the amount of CPS and MWCNT. The electrode was prepared by mixing 1.00 g CPS, 0.125 g MWCNT and 0.125 g PVDF binder (8:1:1 by weight, respectively). After grinding and drying, the mixture was placed in a tablet press and pressed with a pressure of 15 MPa to obtain a sheet-like electrode with an area of 2 × 2 cm^2 and a thickness of 2.4 mm, denoted as the H-CPS-CNT electrode.

Hybrid flow cell assembly and testing

All hybrid flow cells were equipped with graphite flow field plates for electrolyte circulation, a cation-exchange membrane (Nafion NC700) as the separator, a CeTech GF030 carbon felt, a CPS-CNT electrode (geometric surface area 4 cm^2) and two hydrophilic carbon cloths stacked together as the negative electrode. Three hydrophilic carbon cloths were utilized as the positive electrode. Two copper current collectors were used for current collection. In addition, Viton gaskets were used for sealing the hybrid flow cell. The electrolytes consisted of 6 ml of 1.0 M KCl (negative side, capacity limiting) and 40 ml of 0.1 M $K_4Fe(CN)_6$ and 0.02 M $K_3Fe(CN)_6$ in 1.0 M KCl (posolyte, non-capacity limiting). This configuration was denoted as the CPS-CNT flow cell for simplicity. Similarly, for the H-CPS-CNT flow cell, the electrolytes consisted of 6 ml 1.0 M KCl (negative side, capacity limiting) and 40 ml 0.3 M $K_4Fe(CN)_6$ and 0.05 M $K_3Fe(CN)_6$ in 1.0 M KCl (posolyte, non-capacity limiting). Electrolyte flow in all cell evaluations was maintained by a peristaltic pump operating at 110 rpm. All cell tests were performed and monitored under ambient temperature using a BioLogic VSP-300 or BCS-128 instrument.

Electrochemical CO_2 capture and release testing

In the CO_2 capture and release tests, the inlet gas flow rate (5 ml min^{-1}) was regulated using an AST10 DLCMX MFC with a feed gas mixture (N_2, CO_2 and O_2) continuously supplied to the negative chamber at a total pressure of 1 bar. Real-time CO_2 concentration was monitored using a SprintIR 6S-100 CO_2 sensor, while the gas flow rate was monitored by an AST10 DLMMX Flow Meter. The CO_2 sensor was calibrated using standard gases (0–100% CO_2) before testing. Continuous pH monitoring in the electrolyte was recorded using a Mettler-Toledo LE422 pH electrode, with prior calibration performed against standard buffer solutions.

Hybrid flow cell polarization testing

In the hybrid flow cell tests (CPS-CNT electrode as the negative electrode), galvanostatic charge was carried out with 10% of the theoretical capacity as the cut-off condition. After a 15-min stabilization period, OCV was recorded. Potentiostatic electrochemical impedance spectroscopy and CV were subsequently performed. A potentiostatic discharge operation was then performed until the cell was fully discharged. This testing cycle was repeated with 10% increment until reaching full charge (~100% SOC). At each SOC, key parameters such as OCV, potentiostatic electrochemical impedance spectroscopy and CV were recorded sequentially.

Data availability

All data supporting the findings of this study are available within the article and its Supplementary Information. Source data are provided with this paper.

References

1. Sanz-Pérez, E. S., Murdock, C. R., Didas, S. A. & Jones, C. W. Direct capture of CO_2 from ambient air. *Chem. Rev.* **116**, 11840–11876 (2016).
2. McQueen, N. et al. A review of direct air capture (DAC): scaling up commercial technologies and innovating for the future. *Prog. Energy* **3**, 032001 (2021).
3. Lebling, K., Leslie-Bole, H., Byrum, Z. & Bridgwater, L. *Direct Air Capture: 6 Things To Know* (World Resources Institute, 2022).
4. Jin, S., Wu, M., Gordon, R. G., Aziz, M. J. & Kwabi, D. G. pH swing cycle for CO_2 capture electrochemically driven through proton-coupled electron transfer. *Energy Environ. Sci.* **13**, 3706–3722 (2020).
5. Sharifian, R., Wagterveld, R. M., Digdaya, I. A., Xiang, C. & Vermaas, D. A. Electrochemical carbon dioxide capture to close the carbon cycle. *Energy Environ. Sci.* **14**, 781–814 (2021).
6. Renfrew, S. E., Starr, D. E. & Strasser, P. Electrochemical approaches toward CO_2 capture and concentration. *ACS Catal.* **10**, 13058–13074 (2020).
7. Zhu, P. et al. Continuous carbon capture in an electrochemical solid-electrolyte reactor. *Nature* **618**, 959–966 (2023).
8. Kim, S. et al. Asymmetric chloride-mediated electrochemical process for CO_2 removal from oceanwater. *Energy Environ. Sci.* **16**, 2030–2044 (2023).

9. Li, X., Zhao, X. H., Liu, Y. Y., Hatton, T. A. & Liu, Y. Y. Redox-tunable Lewis bases for electrochemical carbon dioxide capture. *Nat. Energy* **7**, 1065–1075 (2022).
10. Voskian, S. & Hatton, T. A. Faradaic electro-swing reactive adsorption for CO_2 capture. *Energy Environ. Sci.* **12**, 3530–3547 (2019).
11. Barlow, J. M. et al. Molecular design of redox carriers for electrochemical CO_2 capture and concentration. *Chem. Soc. Rev.* **51**, 8415–8433 (2022).
12. Stern, M. C., Simeon, F., Herzog, H. & Hatton, T. A. Post-combustion carbon dioxide capture using electrochemically mediated amine regeneration. *Energy Environ. Sci.* **6**, 2505–2517 (2013).
13. Seo, H., Nitzsche, M. P. & Hatton, T. A. Redox-mediated pH swing systems for electrochemical carbon capture. *Acc. Chem. Res.* **56**, 3153–3164 (2023).
14. Cao, T. N.-D. et al. Unraveling the potential of electrochemical pH-swing processes for carbon dioxide capture and utilization. *Ind. Eng. Chem. Res.* **62**, 20979–20995 (2023).
15. Jin, S., Wu, M., Jing, Y., Gordon, R. G. & Aziz, M. J. Low-energy carbon capture via electrochemically induced pH swing with electrochemical rebalancing. *Nat. Commun.* **13**, 2140 (2022).
16. Pang, S. et al. A phenazine-based high-capacity and high-stability electrochemical CO_2 capture cell with coupled electricity storage. *Nat. Energy* **8**, 1126–1136 (2023).
17. Xie, H. et al. Low-energy electrochemical carbon dioxide capture based on a biological redox proton carrier. *Cell Rep. Phys. Sci.* **1**, 100046 (2020).
18. Xie, H. et al. Low-energy-consumption electrochemical CO_2 capture driven by biomimetic phenazine derivatives redox medium. *Appl. Energy* **259**, 114119 (2020).
19. Seo, H. & Hatton, T. A. Electrochemical direct air capture of CO_2 using neutral red as reversible redox-active material. *Nat. Commun.* **14**, 313 (2023).
20. Seo, H., Rahimi, M. & Hatton, T. A. Electrochemical carbon dioxide capture and release with a redox-active amine. *J. Am. Chem. Soc.* **144**, 2164–2170 (2022).
21. Zito, A. M., Bím, D., Vargas, S., Alexandrova, A. N. & Yang, J. Y. Computational and experimental design of quinones for electrochemical CO_2 capture and concentration. *ACS Sustain. Chem. Eng.* **10**, 11387–11395 (2022).
22. Bui, A. T., Hartley, N. A., Thom, A. J. W. & Forse, A. C. Trade-off between redox potential and the strength of electrochemical CO2 capture in quinones. *J. Phys. Chem. C* **126**, 14163–14172 (2022).
23. Lin, K. et al. Alkaline quinone flow battery. *Science* **349**, 1529–1532 (2015).
24. Pohorecki, R. & Moniuk, W. D. W. Kinetics of reaction between carbon dioxide and hydroxyl ions in aqueous electrolyte solutions. *Chem. Eng. Sci.* **43**, 1677–1684 (1988).
25. Keith, D. W., Holmes, G., St. Angelo, D. & Heidel, K. A process for capturing CO_2 from the atmosphere. *Joule* **2**, 1573–1594 (2018).
26. Chen, Q., Eisenach, L. & Aziz, M. J. Cycling analysis of a quinone-bromide redox flow battery. *J. Electrochem. Soc.* **163**, a5057–a5063 (2015).
27. Zuo, P. et al. Near-frictionless ion transport within triazine framework membranes. *Nature* **617**, 299–305 (2023).
28. Yang, G. et al. Organic electroactive materials for aqueous redox flow batteries. *Adv. Mater.* **35**, e2301898 (2023).
29. Pan, L. et al. High-performance porous electrodes for flow batteries: improvements of specific surface areas and reaction kinetics. *ChemElectroChem* **11**, e202400460 (2024).
30. Sun, J. et al. Redox flow batteries and their stack-scale flow fields. *Carbon Neutrality* **2**, 30 (2023).
31. Zhang, Y. et al. Insights into an air-stable methylene blue catholyte towards kW-scale practical aqueous organic flow batteries. *Energy Environ. Sci.* **16**, 231–240 (2023).

Acknowledgements

We thank Y. Tang from Shanghai Institute of Organic Chemistry for helpful discussions. Financial support received from National Natural Science Foundation of China (grant nos. 22422803, 22101064 and 22375167), the open research fund of Suzhou Laboratory (grant no. SZLAB-1308-2024-TS008), the National Key R&D Program of China (grant nos. 2022YFB2405100 and 2022YFB2405000), the Research Funds of Hangzhou Institute for Advanced Study, UCAS (grant no. 2023HIAS-Y018) and Zhejiang Provincial Natural Science Foundation of China (XHD24B0501) is gratefully acknowledged. Research at Harvard University was supported by the Harvard University Climate Change Solutions Fund. We thank the Instrumentation and Service Center for Physical Science at Westlake University for the facility support and technical assistance.

Author contributions

Y.J., M.J.A., P.W. and R.G.G. formulated and supervised the project. X.J. and L.L. synthesized the compounds. X.J. performed the CO_2 capture tests. S.J. performed the theoretical analysis. S.J., Y.J., P.W. and M.J.A. wrote the paper, and all authors contributed to revising the paper.

Competing interests

A patent application (CN202410616404.7) has been filed by Hangzhou Institute for Advanced Study, University of Chinese Academy of Sciences, with Y.J., P.W. and X.J. as inventors.

Additional information

Supplementary information The online version contains supplementary material available at https://doi.org/10.1038/s41560-025-01836-3.

Correspondence and requests for materials should be addressed to Pan Wang, Michael J. Aziz or Yunlong Ji.

Peer review information *Nature Energy* thanks Seoni Kim, Kangkang Li and the other, anonymous, reviewer(s) for their contribution to the peer review of this work.

nature energy

Supplementary information

https://doi.org/10.1038/s41560-025-01836-3

Direct air capture of CO_2 in an electrochemical hybrid flow cell with a spatially isolated phenazine electrode

In the format provided by the authors and unedited

Content

Supplementary Notes

Supplementary Note 1 − Description of the PCET process

(PZ: phenazine; PZH_2: reduced state of phenazine)

Deacidification: $PZ + 2H_2O + 2e^- \rightarrow PZH_2 + 2OH^-$ $Eq.1$

Absorption: $CO_2 + OH^- \rightarrow HCO_3^-$ and $HCO_3^- + OH^- \rightarrow CO_3^{2-} + H_2O$ $Eq.2$

Acidification: $PZH_2 \rightarrow PZ + 2H^+ + 2e^-$ $Eq.3$

Desorption: $CO_3^{2-} + H^+ \rightarrow HCO_3^-$ and $HCO_3^- + H^+ \rightarrow CO_2 + H_2O$ $Eq.4$

Supplementary Note 2 − Synthesis of cyclic poly(phenazine sulfide) (CPS)

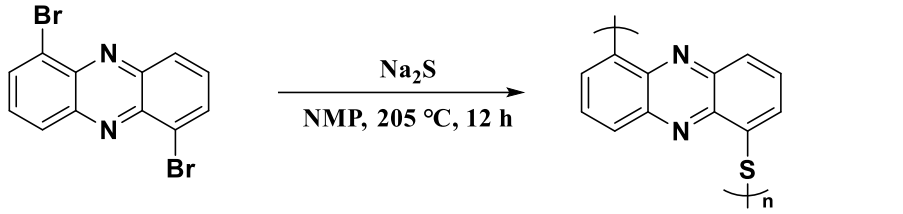

1,6-Dibromophenazines **Cyclic Poly(phenazine sulfide) (CPS)**

1,6-Dibromophenazine was synthesized using a two-step procedure adapted from the previous report.[1] The yield of the two-step was 52%.

To a 150 mL high-pressure flask, 1,6-dibromophenazine (6.76 g, 20 mmol) and anhydrous sodium sulfide (Na_2S, 1.73 g, 20 mmol) were added into 50 mL of 1-methyl-2-pyrrolidone (NMP). The flask was sealed, and the mixture was heated to 205 ℃ with continuous stirring for 12 h under a nitrogen atmosphere. After cooling to room temperature, 500 mL of methanol was added to the reaction solution. The product was collected by filtration, washed with methanol and warm water three times, and then dried under vacuum at 60 ℃ for 24 h to afford a dark green solid in 95% isolated yield.

Supplementary Note 3 − Electrode preparation

Preparation of working electrode for cyclic voltammetry (CV) test:

To prepare the ink, 8.0 mg CPS and 8.0 mg multi-walled carbon nanotubes (MWCNT, LG Chem) were dispersed in a mixture of 100 μL Nafion D-520 solution (5 wt%) and 900 μL isopropanol. The mixture was sonicated for 30 min to form ink solution. The prepared ink was drop-casted onto a glassy carbon electrode with a mass loading of 0.1 mg mm^{-2} (Area: 7 mm^2) and air-dried for 1 h. CV measurements were conducted in a three-electrode system with 20 mV s^{-1} scan rate in various electrolytes, comprising a 3 mm glassy carbon working electrode, a Pt mesh counter electrode, and a Ag/AgCl reference electrode (filled with 3.0 M KCl solution).

Preparation of CPS-CNT electrode as negative electrode for hybrid flow cell:

The electrode was prepared by mixing 0.32 g CPS, 0.32 g MWCNT, and 0.04 g polyvinylidene fluoride (PVDF, Arkema) binder (8 : 8 : 1 by weight, respectively). The mixture was ground in a mortar for 1 h in ethanol to homogenize the particle size and enhance the contact between CPS and MWCNT. After solvent removal by vacuum drying at 60 °C overnight, the resulting powder was placed in a tablet press and pressed with a pressure of 10 MPa to obtain a sheet-like electrode with an area of 2 × 2 cm^2 and a thickness of 1.7 mm, denoted as CPS-CNT electrode.

Following similar procedures described above, a high-capacity CPS-CNT electrode was prepared by controlling the amount of CPS and MWCNT. The electrode was prepared by mixing 1.00 g CPS, 0.125 g MWCNT, and 0.125 g PVDF binder (8 : 1 : 1 by weight, respectively). After grinding and drying, the mixture was placed in a tablet press and pressed with a pressure of 15 MPa to obtain a sheet-like electrode with an area of 2 × 2 cm^2 and a thickness of 2.4 mm, denoted as H-CPS-CNT electrode.

Supplementary Note 4 − Hybrid flow cell assembly and testing

All hybrid flow cells were equipped with graphite flow field plates for electrolyte circulation, a cation exchange membrane (Nafion® NC700) as the separator, a CeTech GF030 carbon felt, a CPS-CNT electrode (geometric surface area 4 cm^2), and two ELAT Hydrophilic carbon cloths stacked together as negative electrode. Three ELAT Hydrophilic carbon cloths were utilized as the positive electrode. Two copper current collectors were used for current collection. In addition, Viton gaskets were used for sealing the hybrid flow cell. The electrolytes were consisted of 6 mL of 1.0 M KCl (negative side, capacity limiting) and 40 mL of 0.1 M $K_4Fe(CN)_6$ and 0.02 M $K_3Fe(CN)_6$ in 1.0 M KCl (posolyte, non-capacity limiting). This configuration was denoted as CPS-CNT flow cell for simplicity. Similarly, for H-CPS-CNT flow cell, the electrolytes were consisted of 6 mL 1.0 M KCl (negative side, capacity limiting) and 40 mL 0.3 M $K_4Fe(CN)_6$ and 0.05 M $K_3Fe(CN)_6$ in 1.0 M KCl (posolyte, non-capacity limiting). Electrolyte flow in all cell evaluations was maintained by a peristaltic pump operating at 110 rpm. All cell tests were performed and monitored under ambient temperature using a BioLogic VSP-300 or BCS-128 instrument.

Supplementary Note 5 − Electrochemical CO_2 capture and release testing

In the CO_2 capture and release tests, the inlet gas flow rate (5 mL min^{-1}) was regulated using an AST10 DLCMX Mass Flow Controller (MFC) with a feed gas mixture (N_2, CO_2, and O_2) continuously supplied to the negative chamber at a total pressure of 1 bar. Real-time CO_2 concentration was monitored using a SprintIR 6S-100 CO_2 sensor, while the gas flow rate was monitored by an AST10 DLMMX Flow Meter. The CO_2 sensor was calibrated using standard gases (0-100% CO_2) prior to testing. Continuous pH monitoring in the electrolyte was recorded using a Mettler-Toledo LE422 pH electrode, with prior calibration performed against standard buffer solutions.

Typical procedure:

Step 1: The cell was charged and deacidificated without feed gas.

Step 2: After deacidification, the pump direction was reversed to direct the solution entirely into the reservoir. Subsequently, the pump and the two valves on the pump line were closed to prevent gas ingress into the cell. Then CO_2 capture process was conducted with the feed gas containing CO_2 at 5 mL min^{-1} (air at a 1 L min^{-1} for DAC cases).

Step 3: After the absorption, the feed gas was changed to 100% CO_2 until the pH variation stabilized and the CO_2 sensor reading reached 100%.

Step 4: The valves and pump were opened to allow the flow of the adsorbent solution, ensuring its contact with the electrodes. The system was then stabilized until a steady-state pH level was reached and the CO_2 sensor reached 100%.

Step 5: The cell was discharged and CO_2 release process was conducted.

Step 6: After the CO_2 release, residual CO_2 gas in the system was removed using a vacuum pump and the system proceeded to the next cycle.

Supplementary Note 6 − CO_2 molar work calculation

The CO_2 molar work (W_{CO2}) is calculated by dividing the net electrical work of the full cycle (W_{cycle}) by ΔDIC according to $Eq.(S5)$. And the W_{cycle} is calculated by combining the work returned during acidification from the work input during deacidification, where $W_{deacidification/acidification}$ can be calculated according to the following $Eq.(S6)$ and U^n is the hybrid flow cell voltage at the nth data recording time t_n, J^n is the current density at the time t_n and A is the active geometric area of 4 cm^2.

$$W_{CO2} = \frac{W_{cycle}}{\Delta DIC} = \frac{W_{deacidfication} + W_{acidification}}{\Delta DIC} \qquad Eq.(S5)$$

$$W_{deacidification/acidification} = \sum_{n=t_i}^{t_f} U^n J^n A \Delta t \qquad Eq.(S6)$$

The $\Delta DIC_{a\to b}$ of a process from state *a* to *b* in the cycle is calculated by subtracting the DIC at state *a* and the DIC at state *b*, as described by the procedure from our previous work.[2] The DIC at any state can be calculated by using the following equations:

$$\text{DIC} = [CO_2(aq)] + [HCO_3^-] + [CO_3^{2-}] \qquad Eq.(S7)$$

$$K_1 = \frac{[HCO_3^-][H^+]}{[CO_2(aq)]} \qquad Eq.(S8)$$

$$K_2 = \frac{[CO_3^{2-}][H^+]}{[HCO_3^-]} \qquad Eq.(S9)$$

$$TA \equiv [OH^-] + [HCO_3^-] + 2[CO_3^{2-}] - [H^+] \qquad Eq.(S10)$$

$$[S^+] - [S^-] = TA \qquad Eq.(S11)$$

$$[H^+][OH^-] = 10^{-14} \qquad Eq.(S12)$$

Where the K_1 and K_2 used here are 1.1×10^{-6} M and 4.1×10^{-10} M,[3] resulting in the first and second pKa for carbonic acid being 6.0 and 9.4, respectively. $Eq.(S11)$ is the definition of TA of the solution under consideration and $Eq.(S11)$ arises from the charge neutrality constraint in solution (S^+ and S^- correspond to the cationic and anionic species of the electrolyte salt). During deacidification, $[S^+]$ increases in the negolyte reservoir, so TA increases as well ($Eq.(S10)$), which means an increase of hydroxide concentration or $[HCO_3^-]$ or $[CO_3^{2-}]$ given nonzero pCO_2 ($Eq.(S11)$). The reverse happens during acidification. The expressions for the concentration of each constituent of DIC can be derived by rearranging the above equations:

$$[CO_2(aq)] = \frac{DIC}{1 + \frac{K_1}{[H^+]} + \frac{K_1 K_2}{[H^+]^2}} \qquad Eq.(S13)$$

$$[HCO_3^-] = \frac{DIC}{1 + \frac{[H^+]}{K_1} + \frac{K_2}{[H^+]}} \qquad Eq.(S14)$$

$$[CO_3^{2-}] = \frac{DIC}{1 + \frac{[H^+]}{K_2} + \frac{[H^+]^2}{K_1 K_2}} \qquad Eq.(S15)$$

Rearranging the equations, we can get an expression relating DIC to TA and $[H^+]$:

$$TA = \frac{10^{-14}}{[H^+]} + \frac{DIC}{1 + \frac{[H^+]}{K_1} + \frac{K_2}{[H^+]}} + 2\frac{DIC}{1 + \frac{[H^+]}{K_2} + \frac{[H^+]^2}{K_1 K_2}} - [H^+] \qquad Eq.(S16)$$

Since K_1 and K_2 are constants, inputting the values for $[H^+]$ (derived from pH) and TA, obtained through $Eq.(S11)$ or correlating with charges passed during deacidification or acidification, the DIC value at the state can be solved numerically.

Because the deviation from the baseline in Supplementary Figures 46E and 47E is solely caused by CO_2 absorption, the amount of CO_2 captured is calculated by integrating the difference between the recorded flow rate and the baseline.

$$Q_{CO2} = \sum_{n=t_i}^{t_f} \left|(V_{CO2} - V_{CO2}^{base})\right| \Delta t \qquad Eq.(S17)$$

Where V_{CO2} (mL min^{-1}) is the real-time flow rate of CO_2, Q_{CO2} (mL) is the amount of CO_2 absorbed or released, V_{CO2}^{base} is the baseline CO_2 flow rate, t_i is the start time of capture or release, t_f is the final time of capture or release, Δt (min) is the time difference between successive measurements. V_{CO2} and Q_{CO2} are reckoned at T = 293.15 K and P = 1 bar.

Supplementary Figures

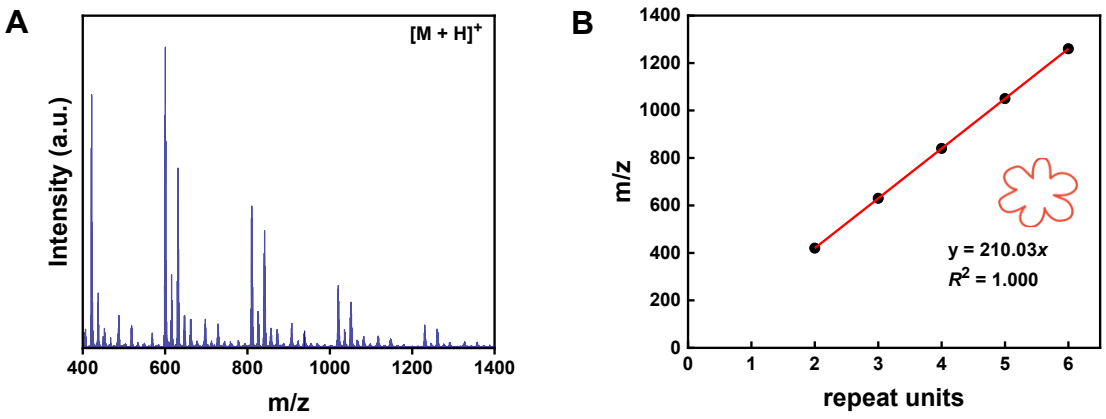

Supplementary Figure 1. (A) MALDI TOF mass spectrometry of CPS after the Soxhelt extraction. The main chain was 2 - 6 units long, including $[M + H]^+$ 420.05, 630.08, 840.10, 1050.12, 1260.15. (B) Linear plot of m/z values vs the number of CPS repeat units. The data points were fitted with a line using a linear fit, where $y = 210.03x$, $R^2 = 1$.

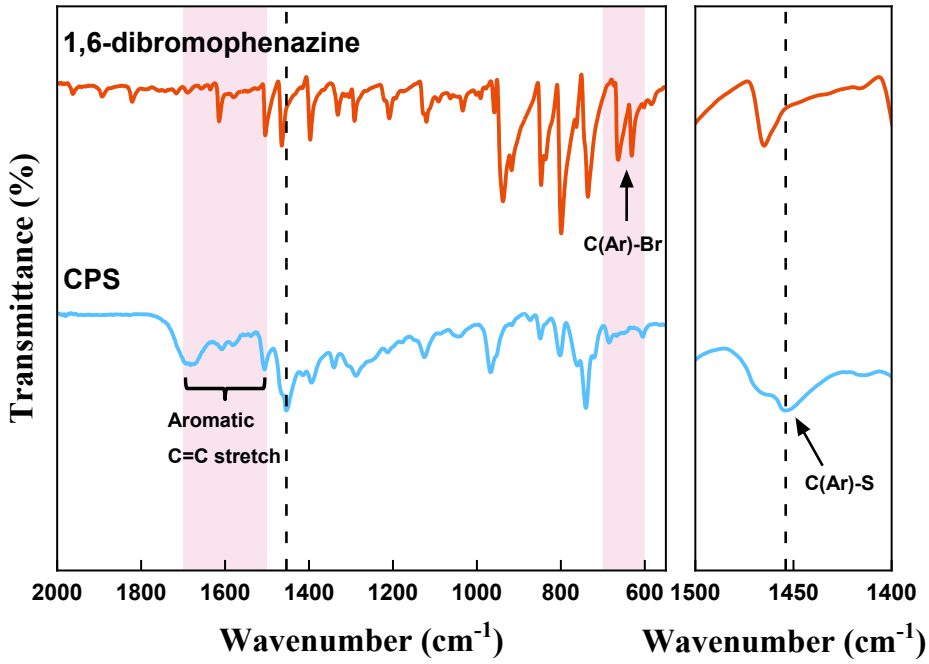

Supplementary Figure 2. FTIR spectra of the monomer (1,6-dibromophenazine) and CPS macrocycles.

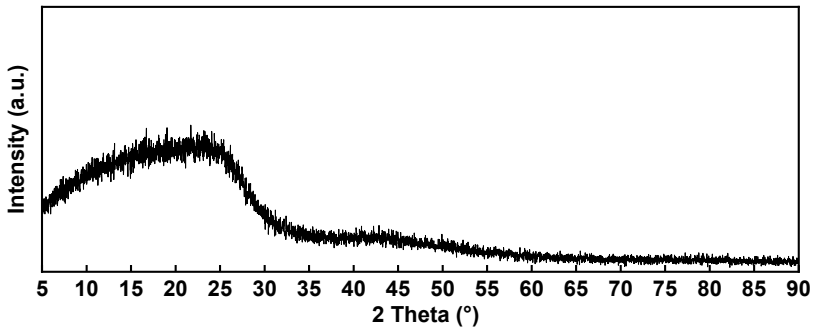

Supplementary Figure 3. Powder-XRD patterns of CPS.

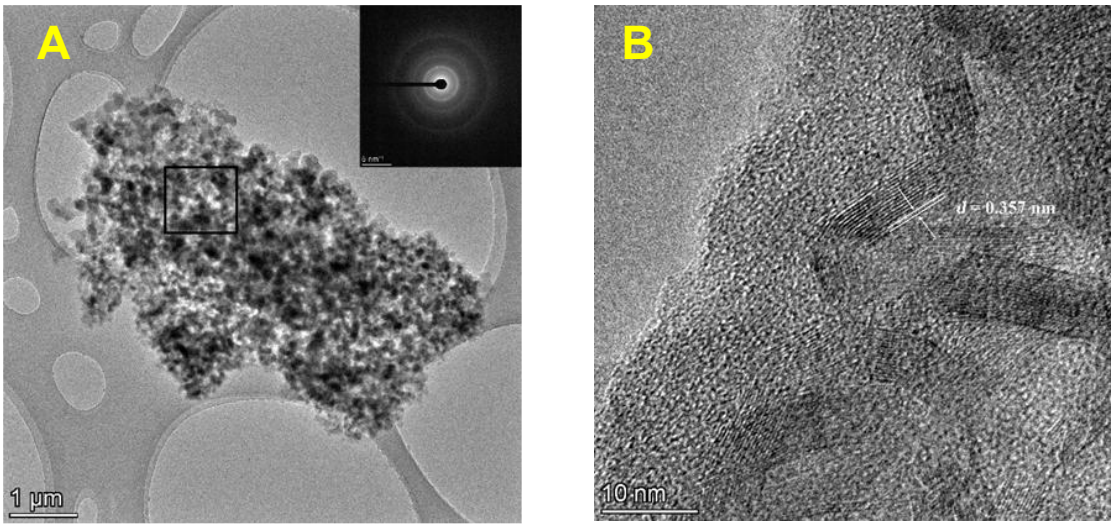

Supplementary Figure 4. HR-TEM images of CPS at different magnifications. The scale bar is (A) 1 μm, (B) 10 nm.

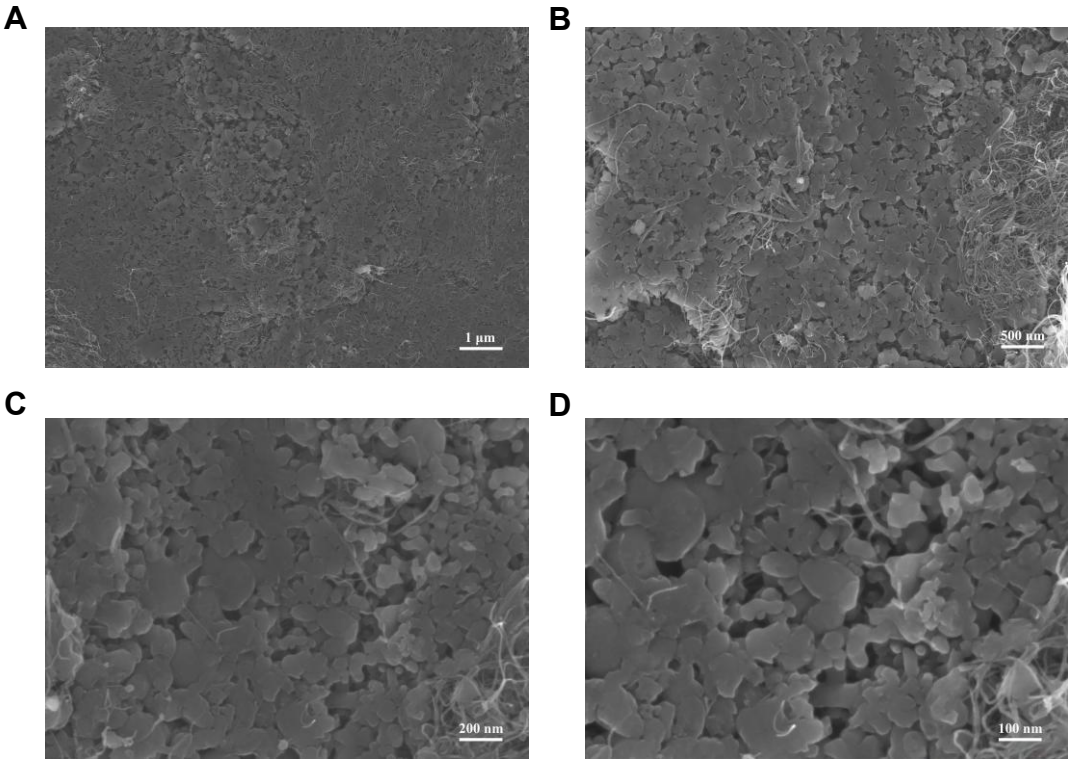

Supplementary Figure 5. SEM images of CPS-CNT electrode at different magnifications. The scale bar was (A) 1 µm, (B) 500 nm, (C) 200nm, (D) 100nm.

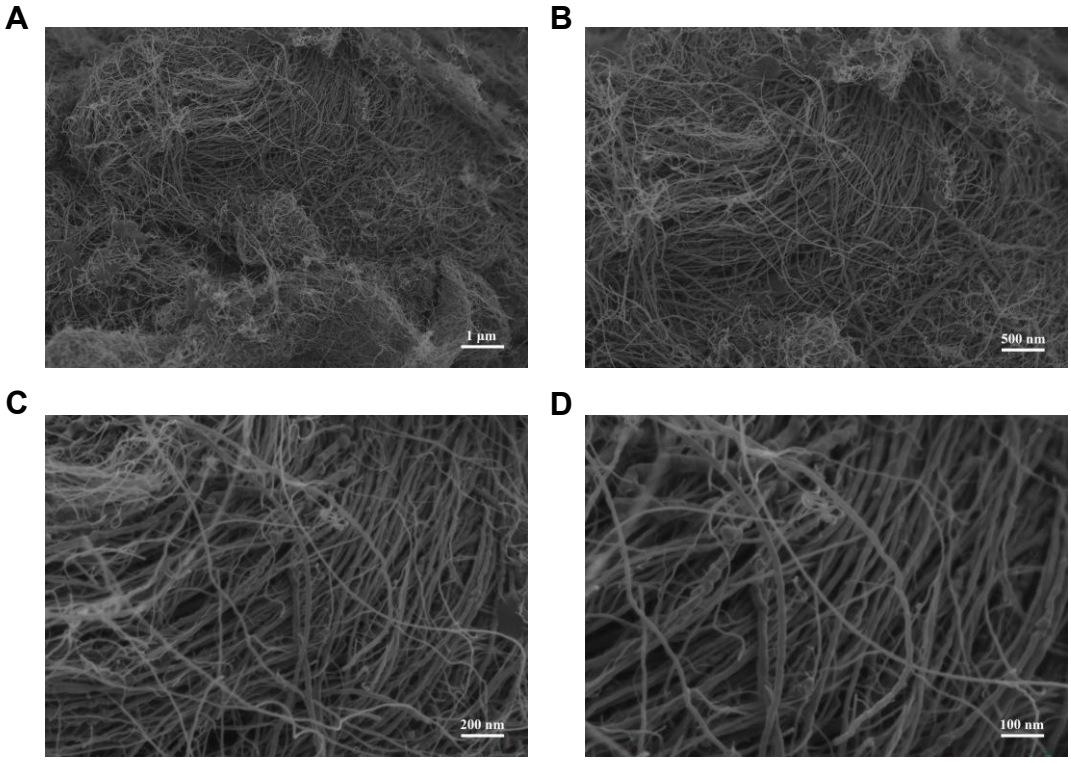

Supplementary Figure 6. SEM images of MWCNT + PVDF (MWCNT/ PVDF = 8 : 1 by weight, respectively) at different magnifications. The scale bar was (A) 1 µm, (B) 500 nm, (C) 200nm, (D) 100nm.

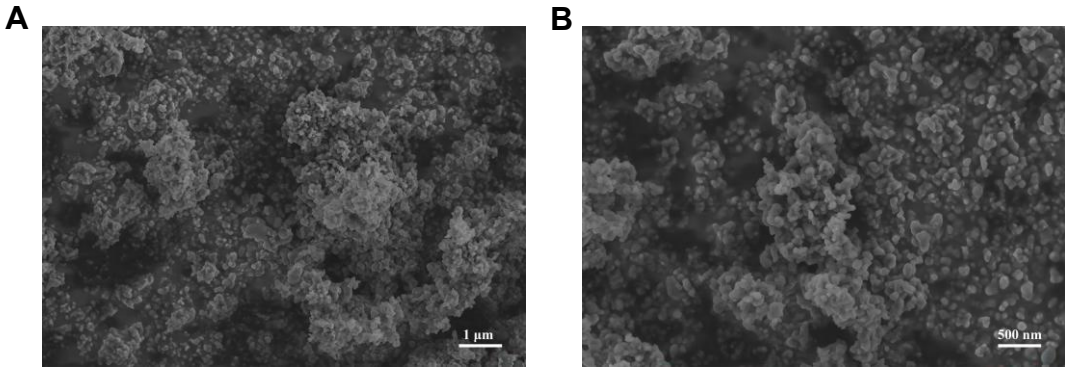

Supplementary Figure 7. SEM images of CPS at different magnifications. The scale bar was (A) 1 μm, (B) 500 nm.

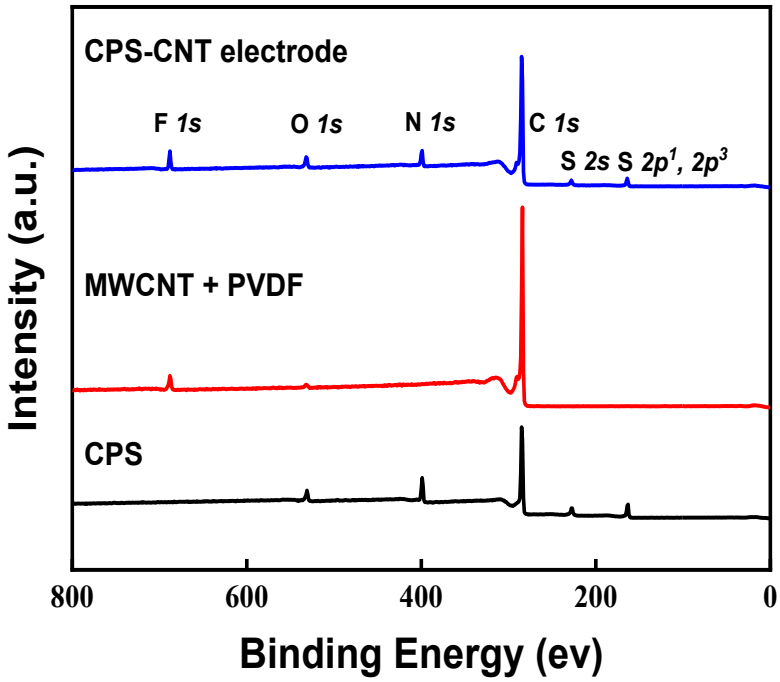

Supplementary Figure 8. XPS spectrum of CPS-CNT electrode, MWCNT + PVDF, and CPS.

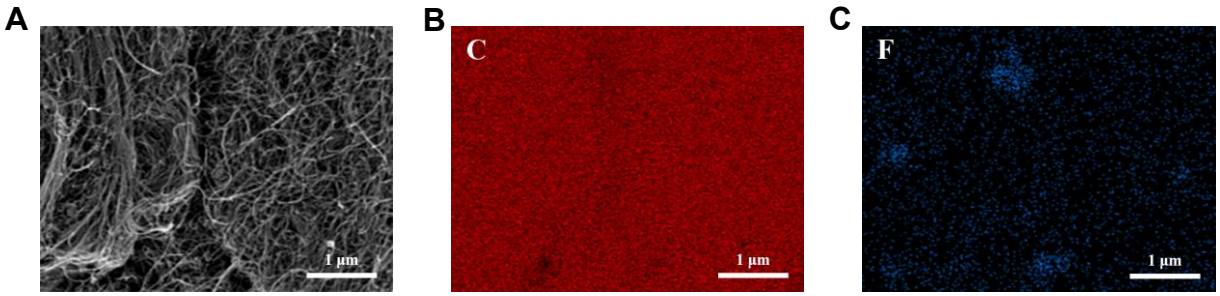

Supplementary Figure 9. (A) Typical SEM image, and corresponding EDS elemental maps of (B) Carbon, (C) Fluorine in MWCNT + PVDF (MWCNT/PVDF = 8 : 1 by weight, respectively) with a scale bar of 1 μm.

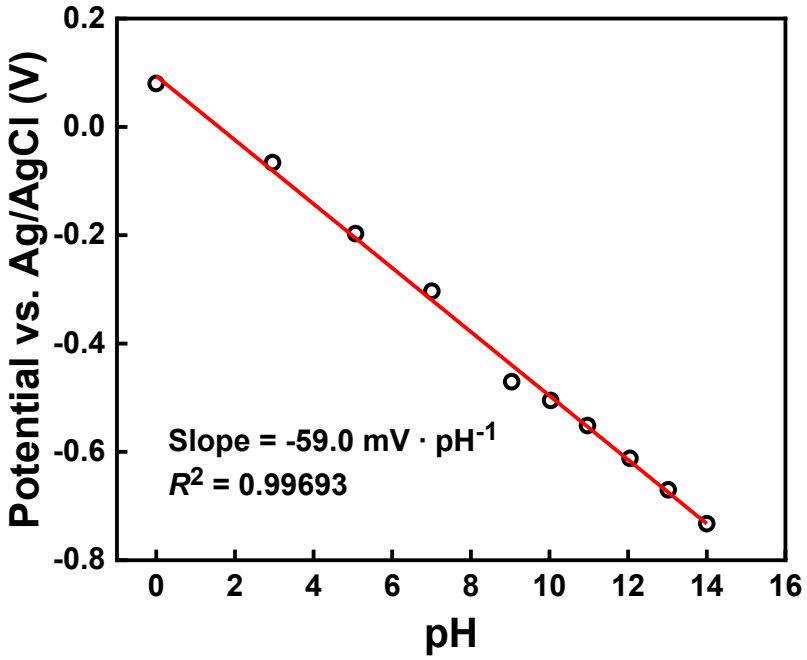

Supplementary Figure 10. Pourbaix diagram of CPS/CNT with a slope of -59.0 mV/pH at different pH values. The data points were fitted with a line using a linear fit, where $y = -0.05902x + 0.09383$, $R^2 = 0.99693$. All the potentials were determined by cyclic voltammetry of CPS/CNT in buffered solutions.

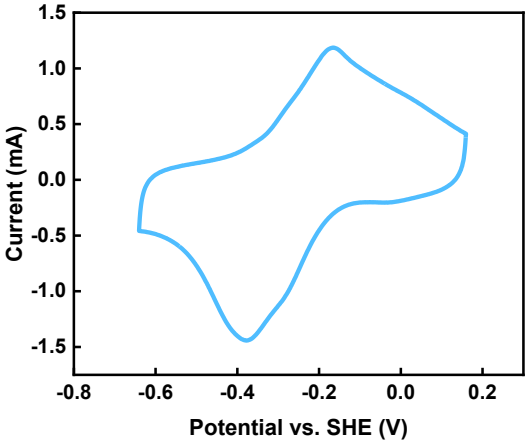

Supplementary Figure 11. CV curve of CPS/CNT in 0.4 M K_2CO_3 and 0.1 M $KHCO_3$ of 1.0 M KCl solution under CO_2 atmosphere.

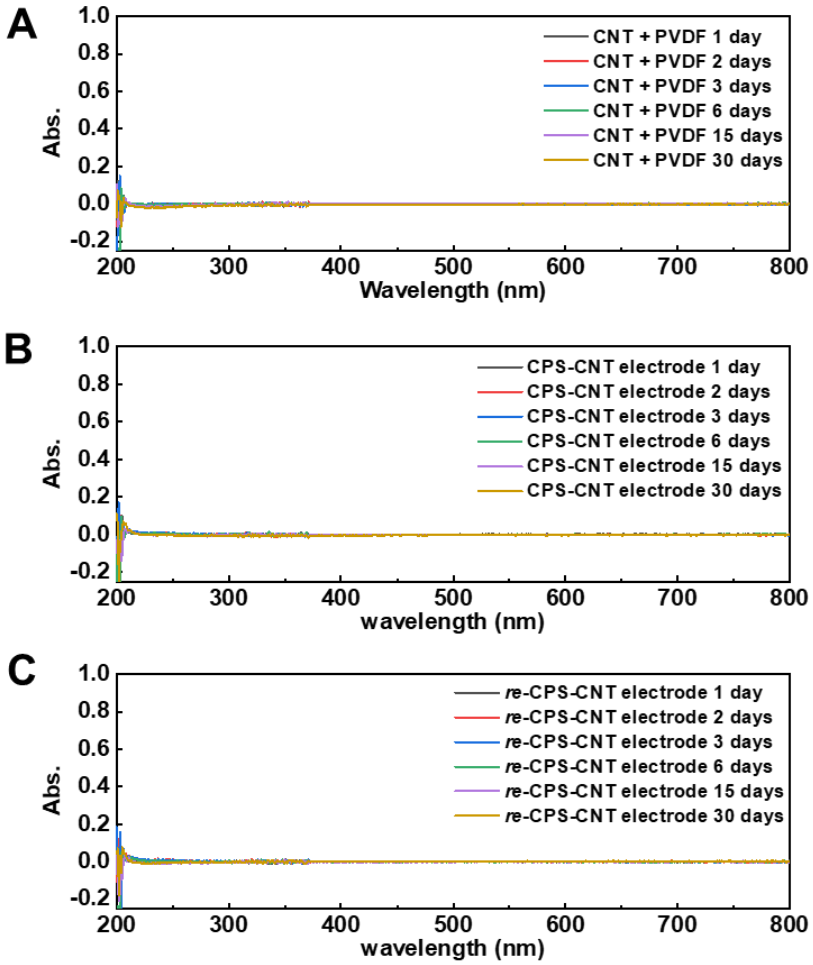

Supplementary Figure 12. UV-vis spectra of the soaking solution with (A) the background electrode (CNT + PVDF), (B) CPS-CNT electrode, and (C) *re*-CPS-CNT electrode after soaking in 1.0 M KCl aqueous solution for varying durations: 1 day, 2 days, 3 days, 6 days, 15 days and 30 days.

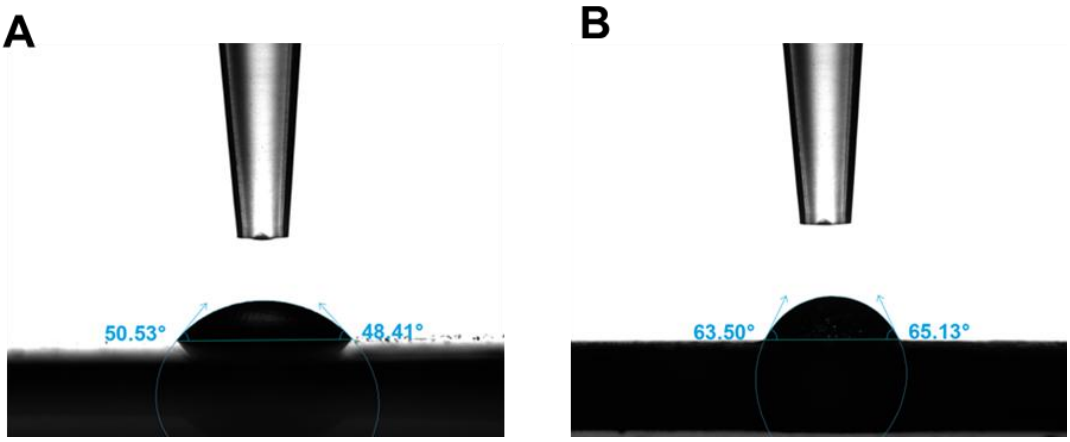

Supplementary Figure 13. Contact angle of (A) CPS (pressed into a sheet-like form) and (B) CPS-CNT electrode with PVDF as a binder.

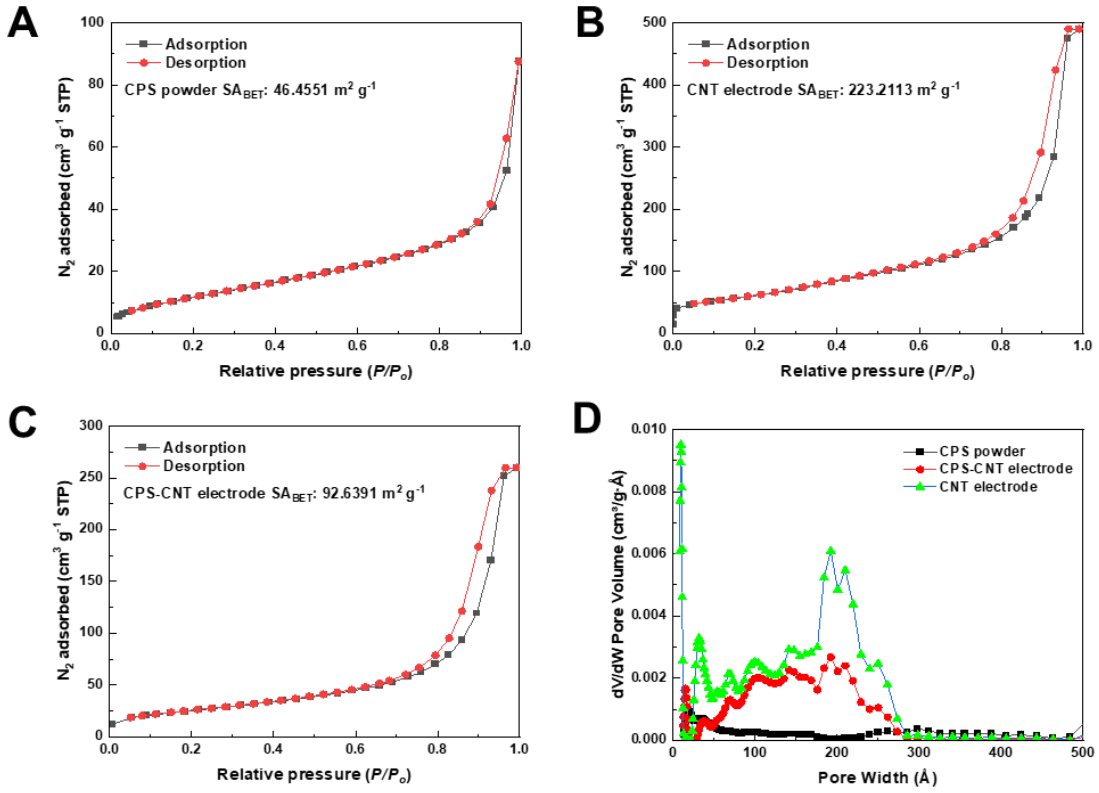

Supplementary Figure 14. N_2 adsorption-desorption isotherms at 77 K of (A) CPS powder, (B) CNT electrode with PVDF as the binder, and (C) CPS-CNT electrode, with PVDF as the binder. (D) Pore size distribution based on DFT pore analysis.

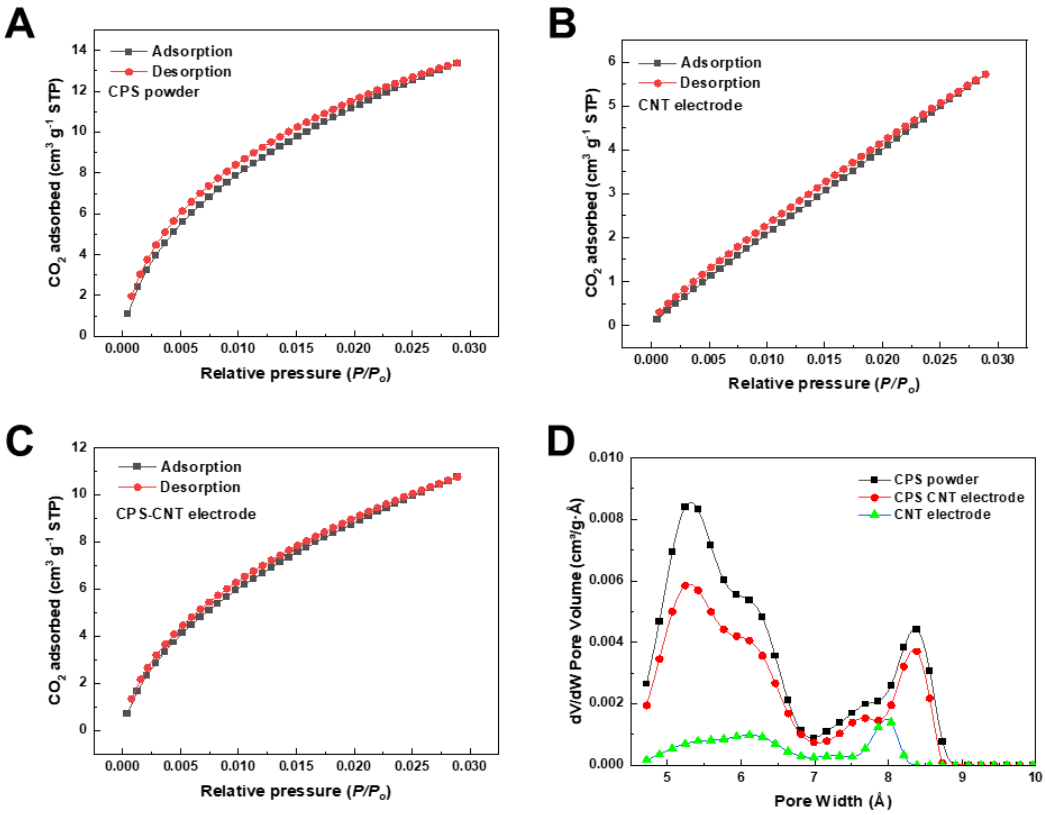

Supplementary Figure 15. CO_2 adsorption-desorption isotherms at 273 K of (A) CPS powder, (B) CNT electrode with PVDF as the binder, and (C) CPS-CNT electrode, with PVDF as the binder. (D) Pore size distribution based on DFT pore analysis.

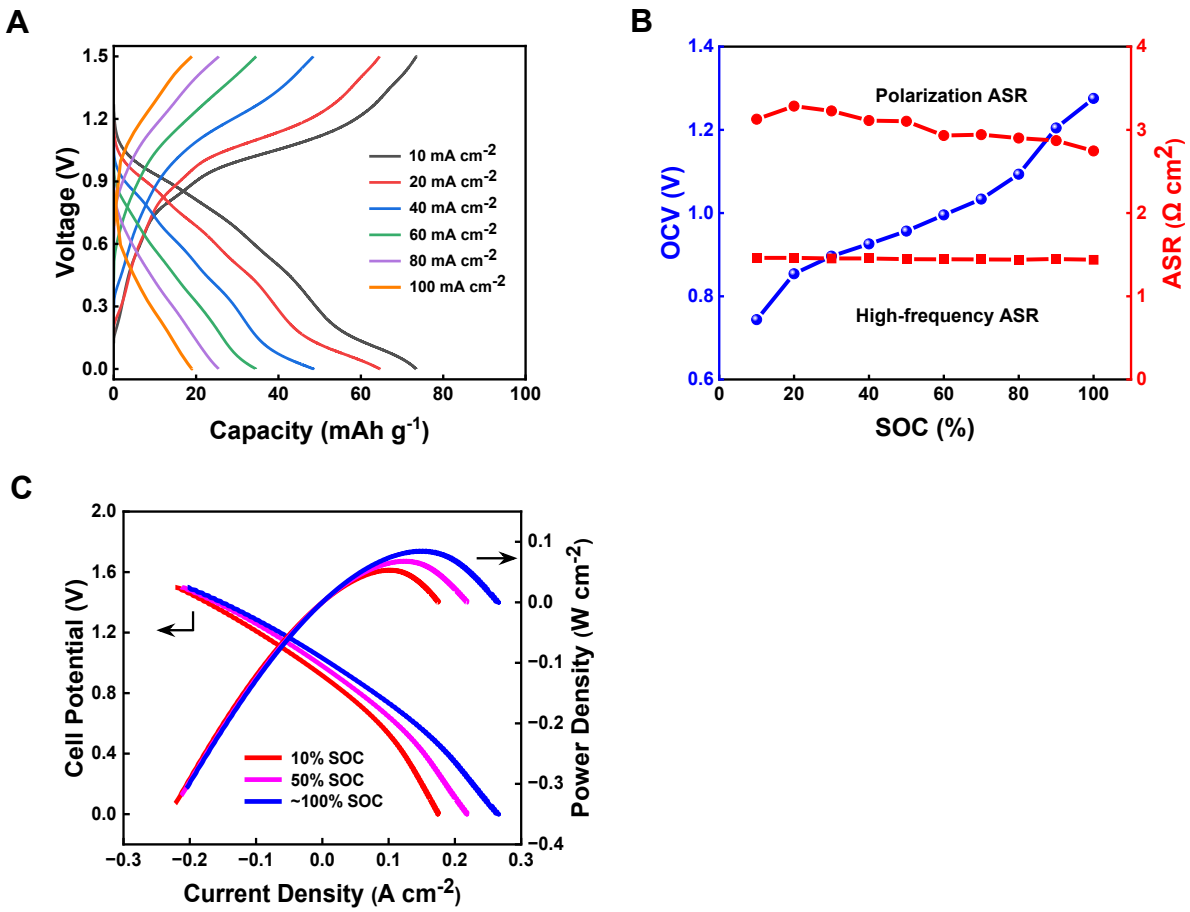

Supplementary Figure 16. (A) The capacity and galvanostatic charge-discharge voltage profiles at various current densities. (B) Full cell OCV, high-frequency and polarization ASR versus various SOCs. (C) Cell potential and power density versus current density at 10%, 50%, and ca. 100% SOC.

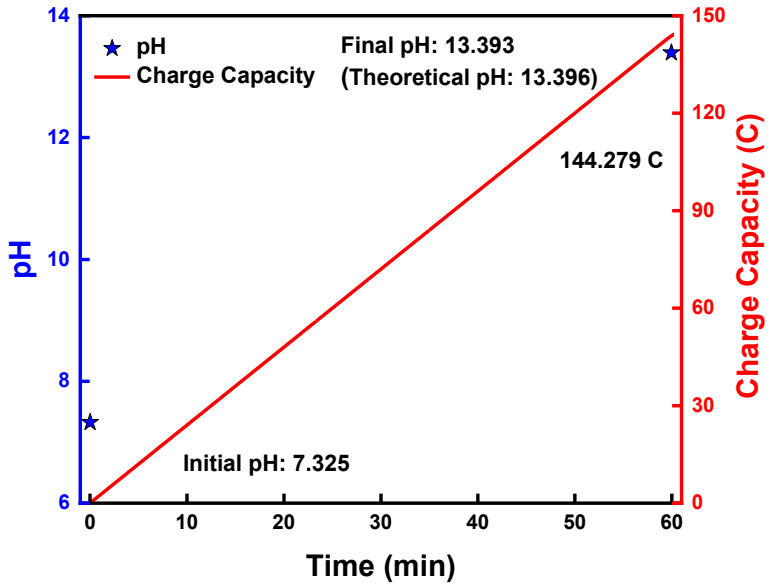

Supplementary Figure 17. Changes of pH and charge capacity before and after cell charging.

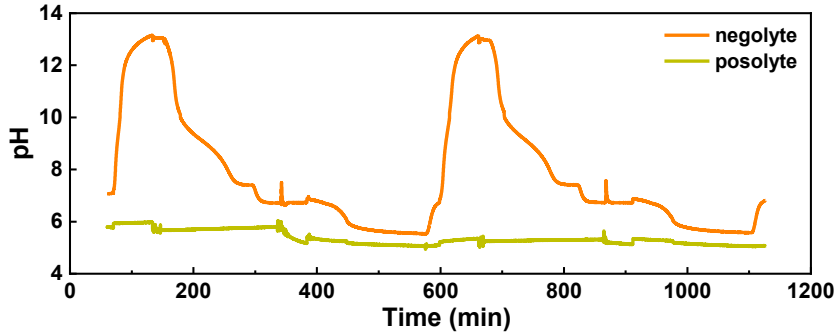

Supplementary Figure 18. pH at the negolyte and posolyte during charge/discharge cycles.

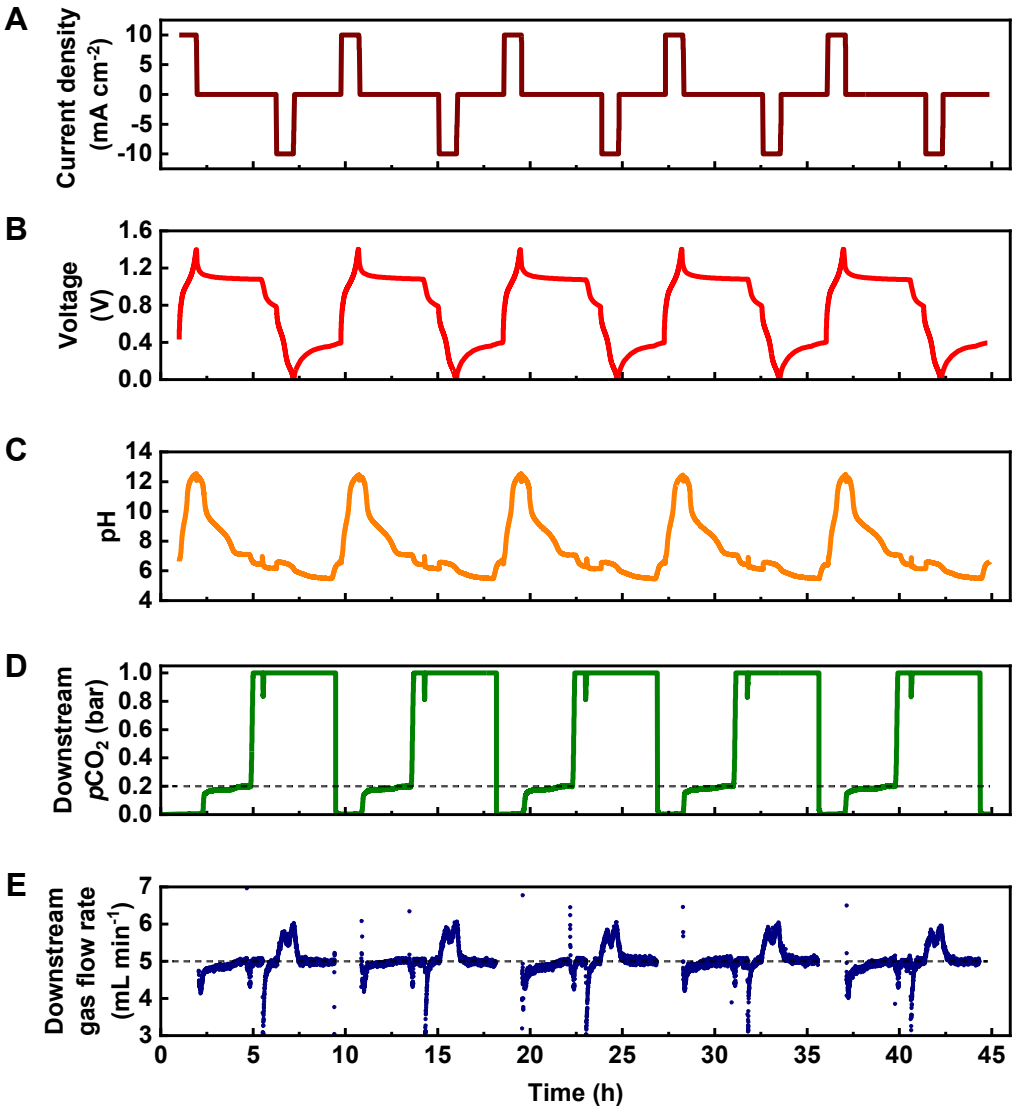

Supplementary Figure 19. Five CO_2 concentrating cycles with CPS-CNT flow cell. The cell was cycled galvanostatically at 10 mA cm^{-2} with a voltage cut-off between 1.4 V and 0.0 V and each half cycle ended with a potentiostatic hold until the magnitude of the current density fell below 7.5 mA cm^{-2} (charge) and 5 mA cm^{-2} (discharge). No feed gas was used during the deacidification process. The gas containing 20% CO_2, 20% O_2, and 60% N_2 was fed during the whole capture step, pure CO_2 was fed during the whole acidification and sweep step. After each cycle, residual CO_2 gas in the pipeline was evacuated using a vacuum pump. The initial gas flow rate was set to 5 mL min^{-1}. (A) Current density. (B) Voltage. (C) pH of the negolyte. (D) Downstream CO_2 partial pressure. The black dashed baseline indicates pCO_2 = 0.2 bar. (E) Downstream total gas flow rate. The black dashed baseline is 5 mL min^{-1}.

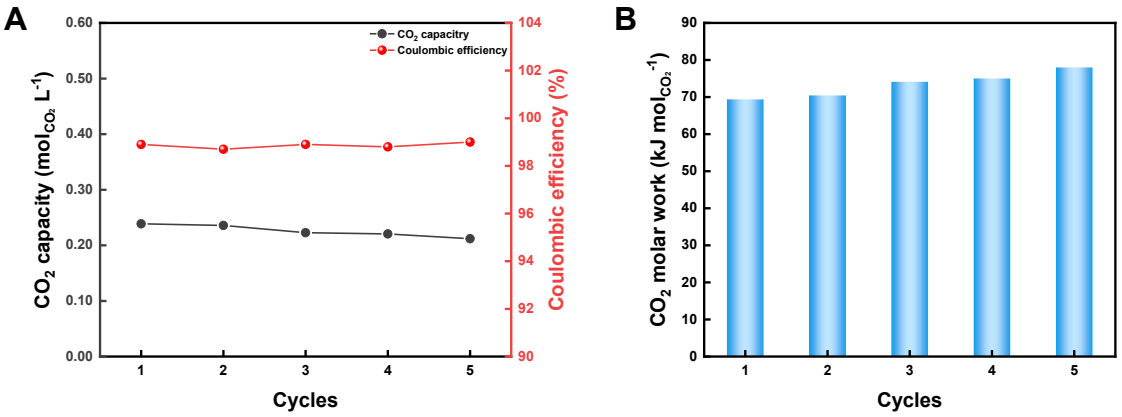

Supplementary Figure 20. (A) CO_2 capacity, coulombic efficiency, (B) CO_2 molar work for each cycle illustrated in the cycles for capture from 20% CO_2, 20% O_2, and 60% N_2 reported in Supplementary Figure 19.

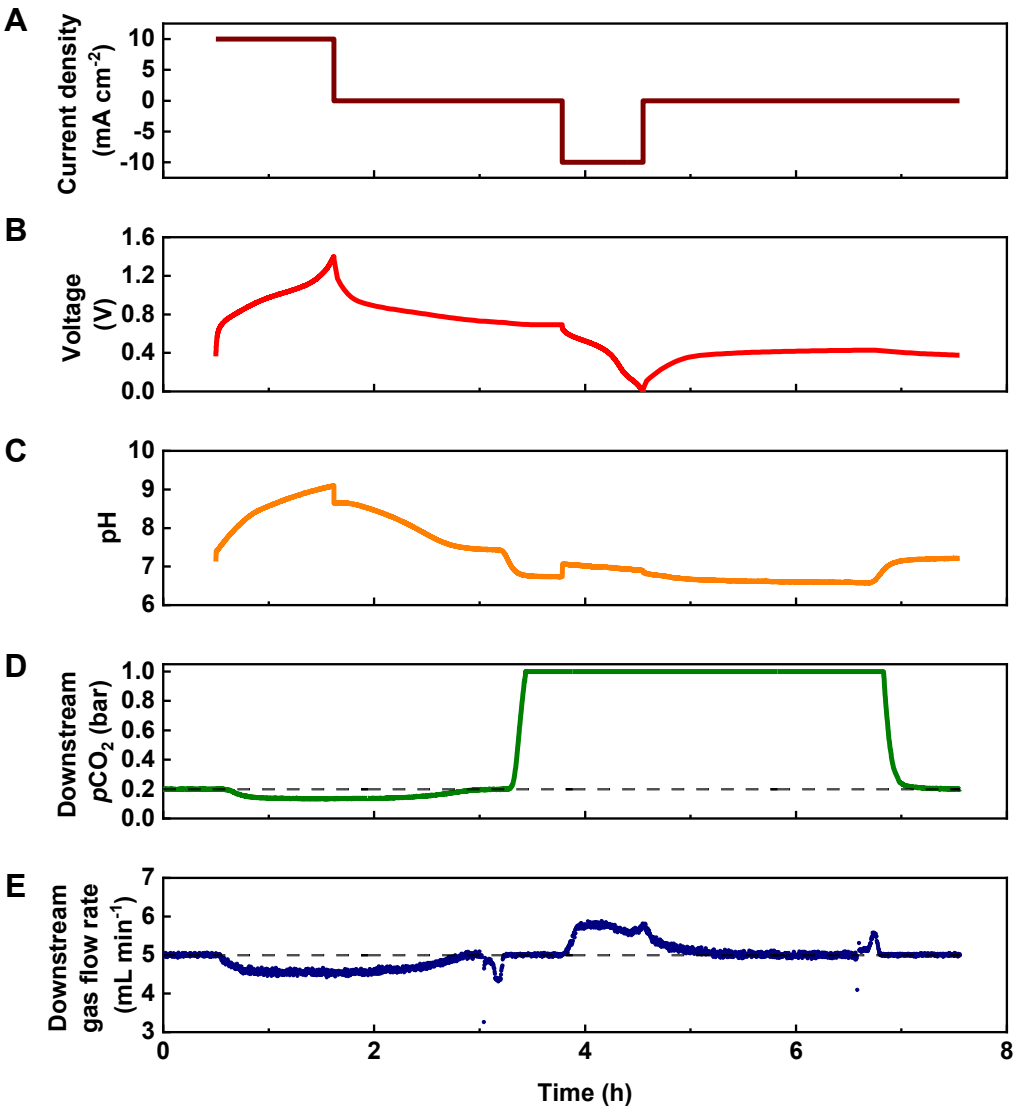

Supplementary Figure 21. One full CO_2 concentrating cycle with CPS-CNT flow cell. The cell was cycled galvanostatically at 10 mA cm^{-2} with a voltage cut-off between 1.4 V and 0.0 V. The gas containing 20% CO_2, 20% O_2, and 60% N_2 was fed during the whole deacidification and capture step, pure CO_2 was fed during the whole acidification and sweep step. The initial gas flow rate was set to 5 mL min^{-1}. (A) Current density. (B) Voltage. (C) pH of the negolyte. (D) Downstream CO_2 partial pressure. The black dashed baseline indicates pCO_2 = 0.2 bar. (E) Downstream total gas flow rate. The black dashed baseline is 5 mL min^{-1}.

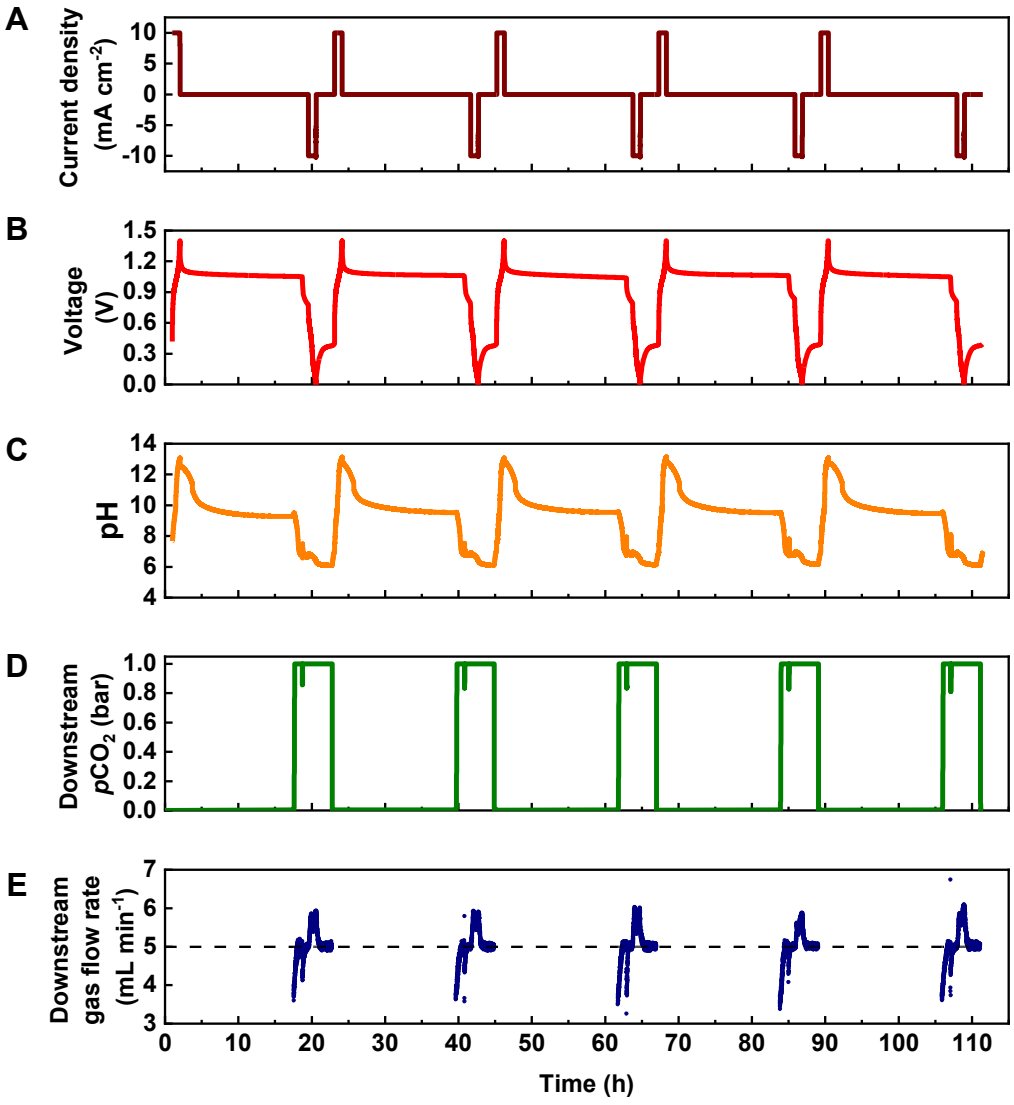

Supplementary Figure 22. Five CO_2 concentrating cycles with CPS-CNT flow cell, which captured CO_2 from air. The cell was cycled galvanostatically at 10 mA cm^{-2} with a voltage cut-off between 1.4 V and 0.0 V and each half cycle ended with a potentiostatic hold until the magnitude of the current density fell below 7.5 mA cm^{-2} (charge) and 5 mA cm^{-2} (discharge). No feed gas was used during the deacidification process. The feed gas was air at 1 L min^{-1} flow rate for the capture step (15 h) and switched to pure CO_2 at 5 mL min^{-1} for the whole acidification and sweep step. After each cycle, residual CO_2 gas in the pipeline was evacuated using a vacuum pump. (A) Current density. (B) Voltage. (C) pH of the negolyte. (D) Downstream CO_2 partial pressure. (E) Downstream total gas flow rate. The black dashed baseline is 5 mL min^{-1}.

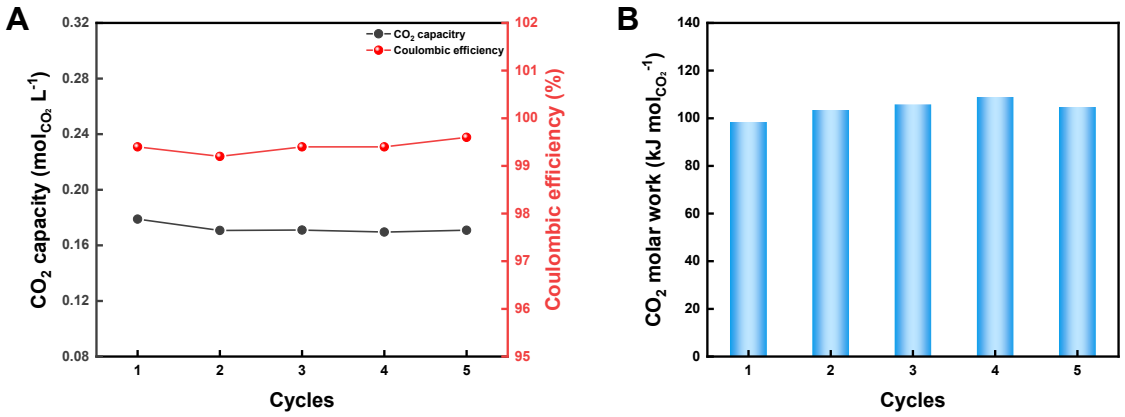

Supplementary Figure 23. (A) CO_2 capacity, coulombic efficiency, (B) CO_2 molar work for each cycle illustrated in the direct air capture cycles reported in Supplementary Figure 22.

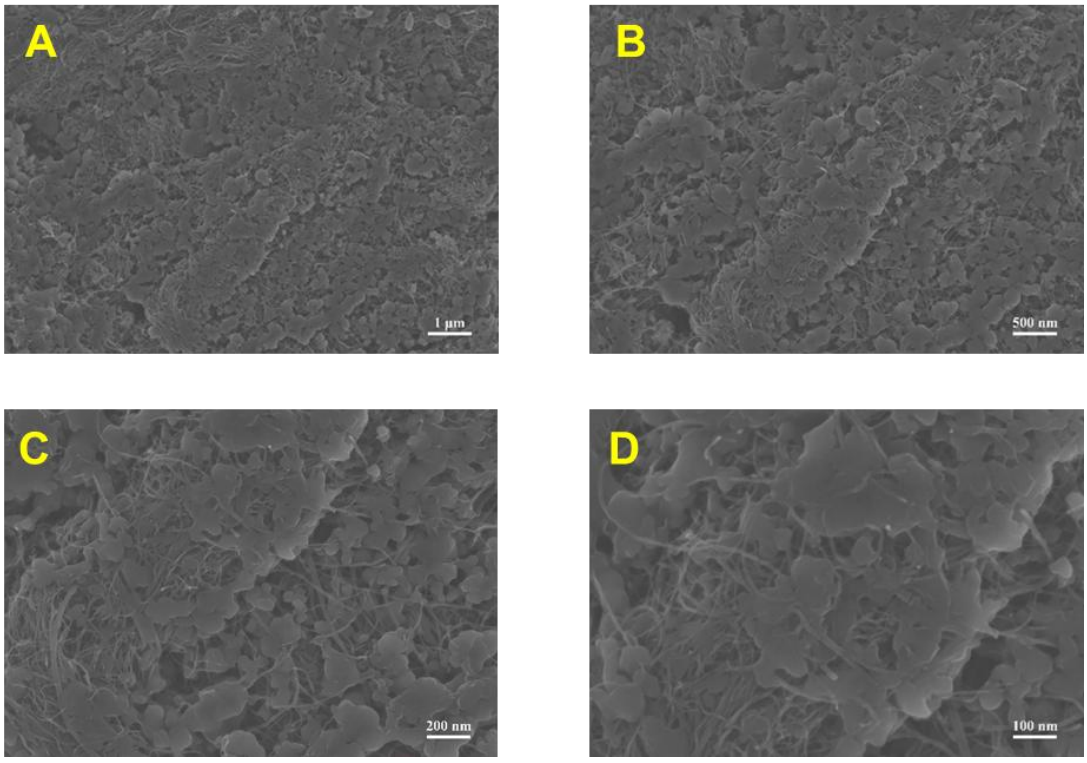

Supplementary Figure 24. SEM images of CPS-CNT electrode at different magnifications after five consecutive cycles of capturing airborne CO_2. The scale bar was (A) 1 µm, (B) 500 nm, (C) 200nm, (D) 100nm.

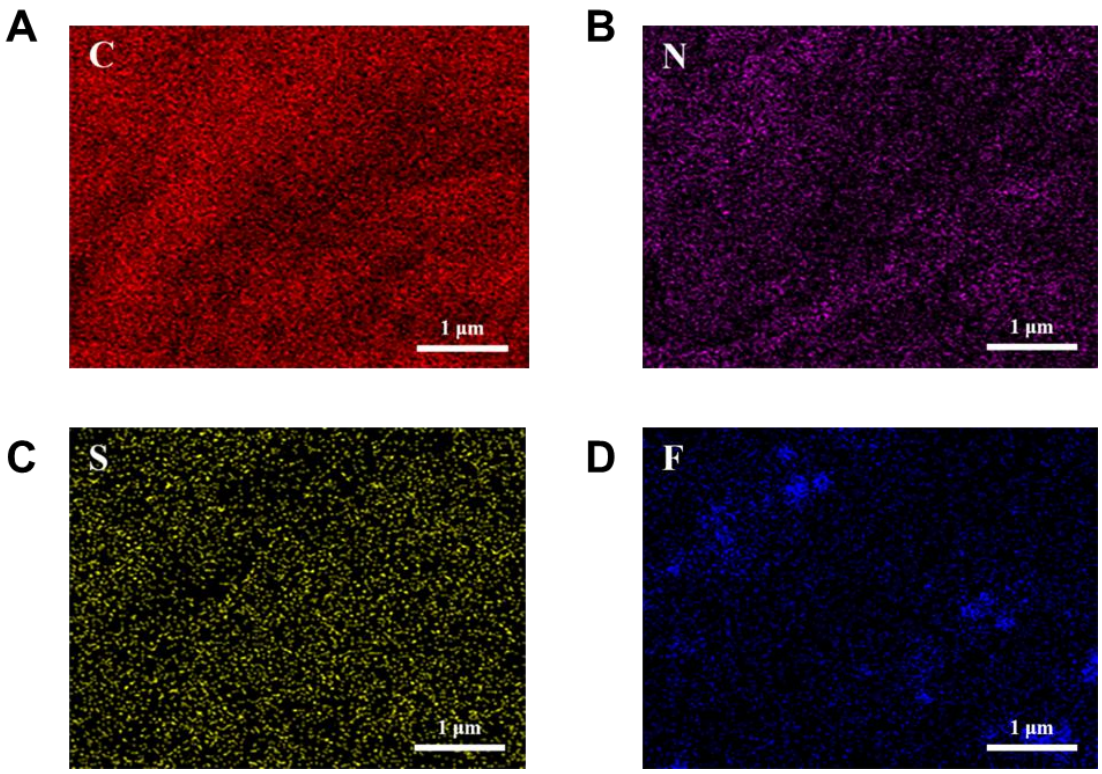

Supplementary Figure 25. Corresponding EDS elemental maps of (A) Carbon, (B) Nitrogen, (C) Sulfur, (D) Fluorine in CPS-CNT electrode with a scale bar of 1 µm after five consecutive cycles of capturing airborne CO_2.

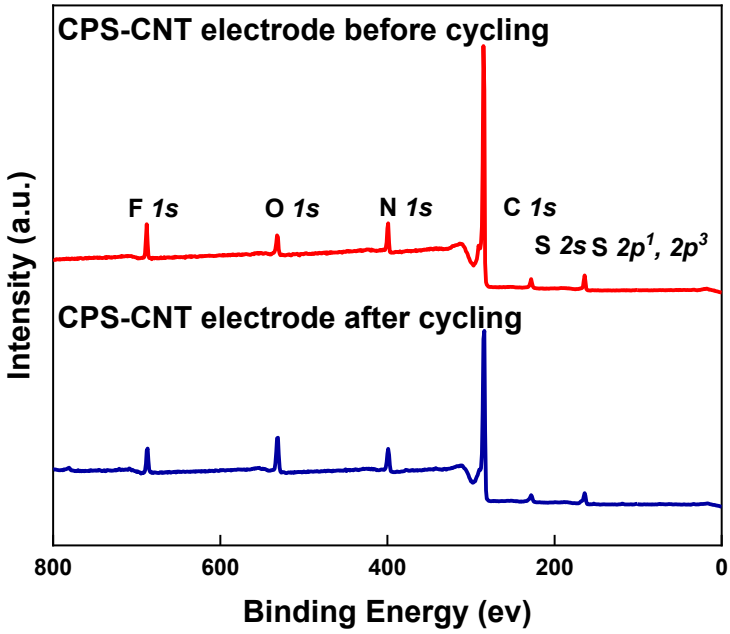

Supplementary Figure 26. XPS spectrum of CPS-CNT electrode before cycling and after cycling.

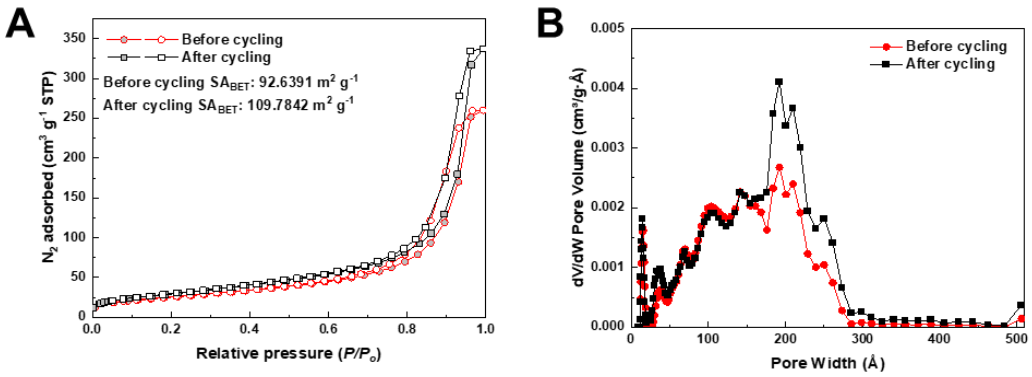

Supplementary Figure 27. N_2 adsorption-desorption isotherms at 77 K of (A) CPS-CNT electrode, with PVDF as the binder. (B) Pore size distribution based on DFT pore analysis.

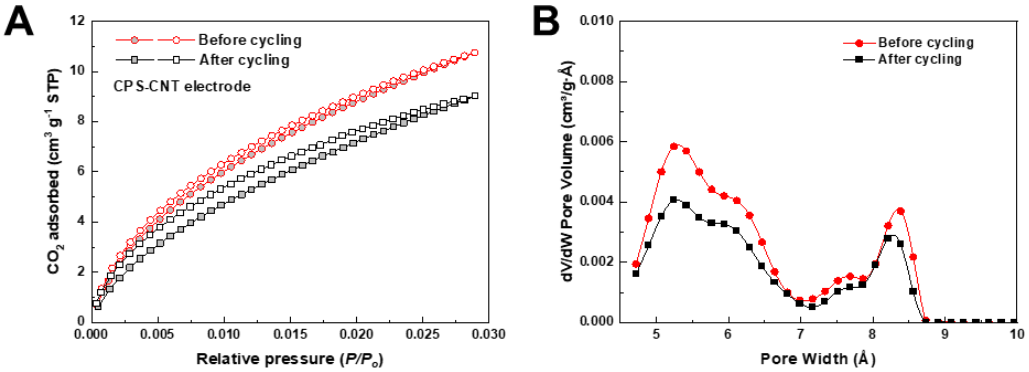

Supplementary Figure 28. CO_2 adsorption-desorption isotherms at 273 K of (A) CPS-CNT electrode, with PVDF as the binder. (B) Pore size distribution based on DFT pore analysis.

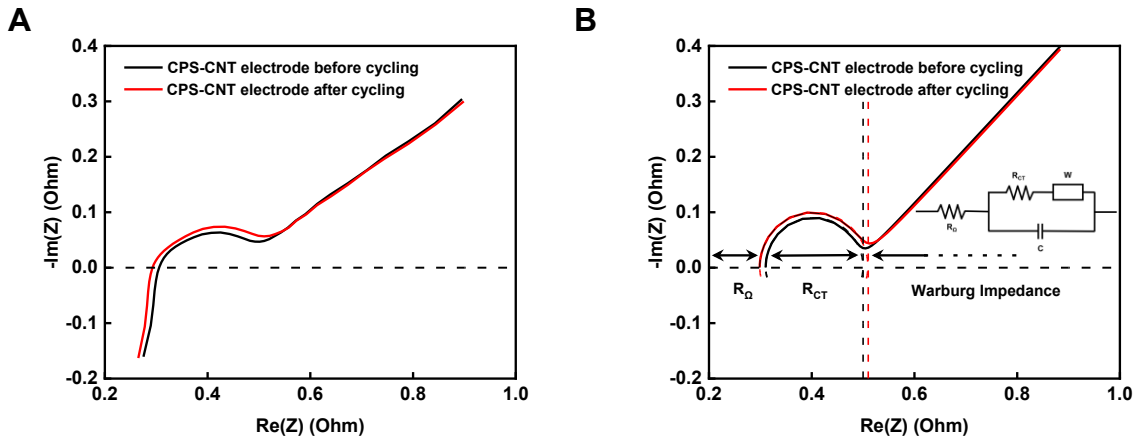

Supplementary Figure 29. (A) Nyquist impedance spectra of CPS-CNT electrode before and after cycling. (B) Fit the Nyquist plot with an equivalent circuit model.

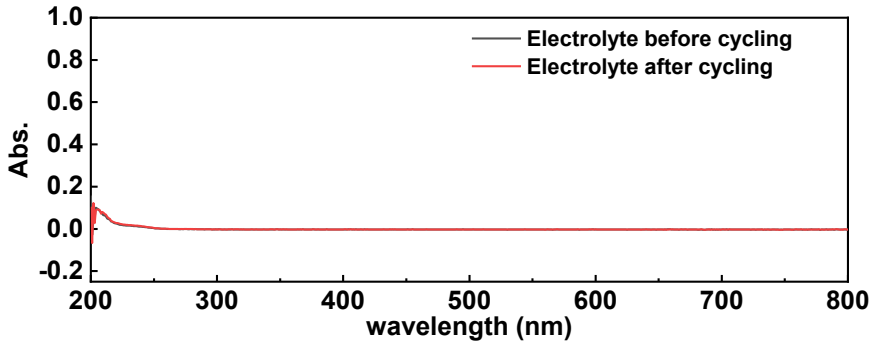

Supplementary Figure 30. UV-vis spectra of the electrolyte before and after cycling.

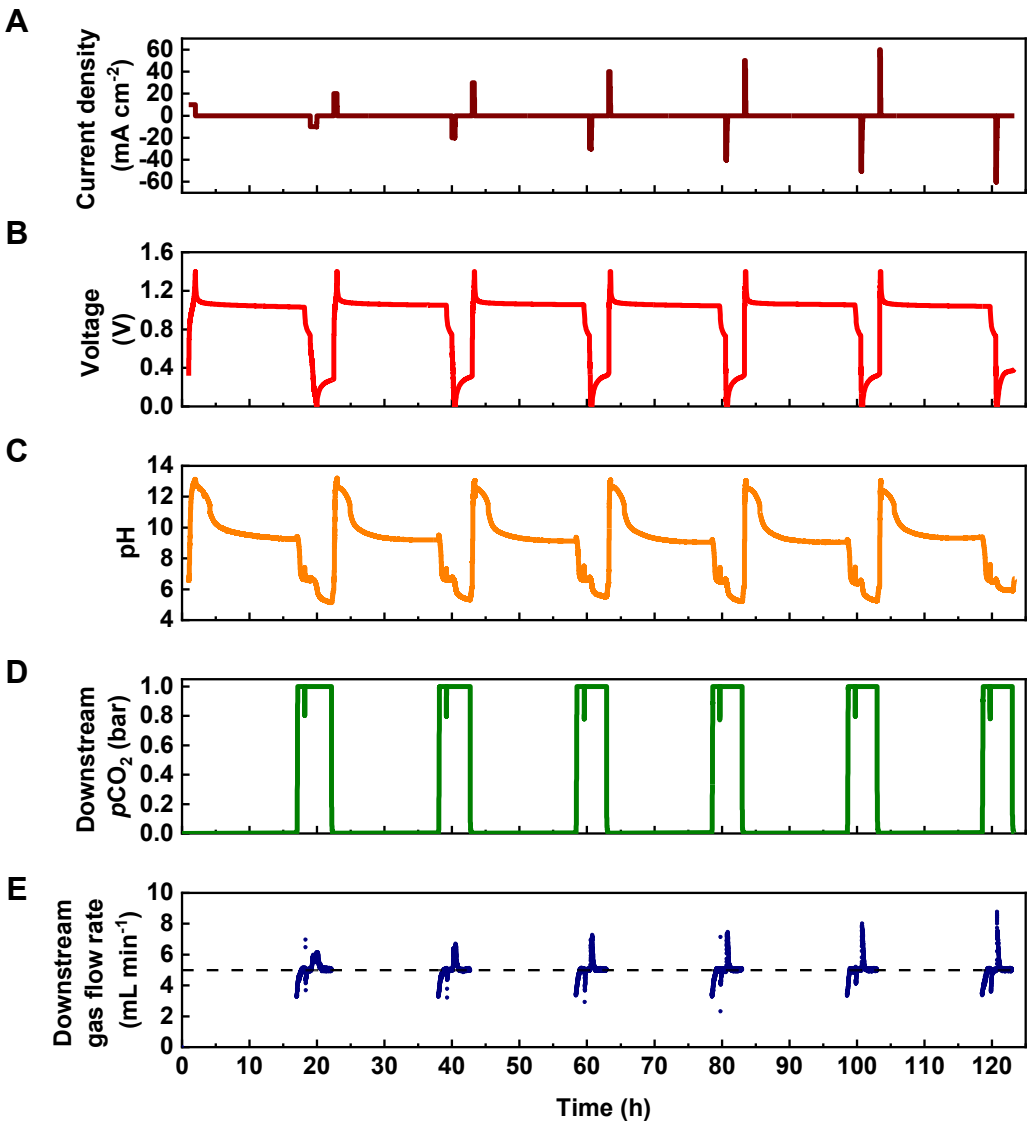

Supplementary Figure 31. Six full direct air CO_2 capture and release cycles with CPS-CNT flow cell at 10 mA cm^{-2} (1st), 20 mA cm^{-2} (2nd), 30 mA cm^{-2} (3rd), 40 mA cm^{-2} (4th), 50 mA cm^{-2} (5th), 60 mA cm^{-2} (6th), respectively. The cell was cycled galvanostatically at 10 to 60 mA cm^{-2} with a voltage cut-off between 1.4 V and 0.0 V and each half cycle ended with a potentiostatic hold until the magnitude of the current density fell below 7.5 mA cm^{-2} (charge) and 5 mA cm^{-2} (discharge). No feed gas was used during the deacidification process. The feed gas was air at 1 L min^{-1} flow rate for the capture step (15 h) and switched to pure CO_2 at 5 mL min^{-1} for the whole acidification and sweep step. After each cycle, residual CO_2 gas in the pipeline was evacuated using a vacuum pump. (A) Current density. (B) Voltage. (C) pH of the negolyte. (D) Downstream CO_2 partial pressure. (E) Downstream total gas flow rate. The black dashed baseline is 5 mL min^{-1}.

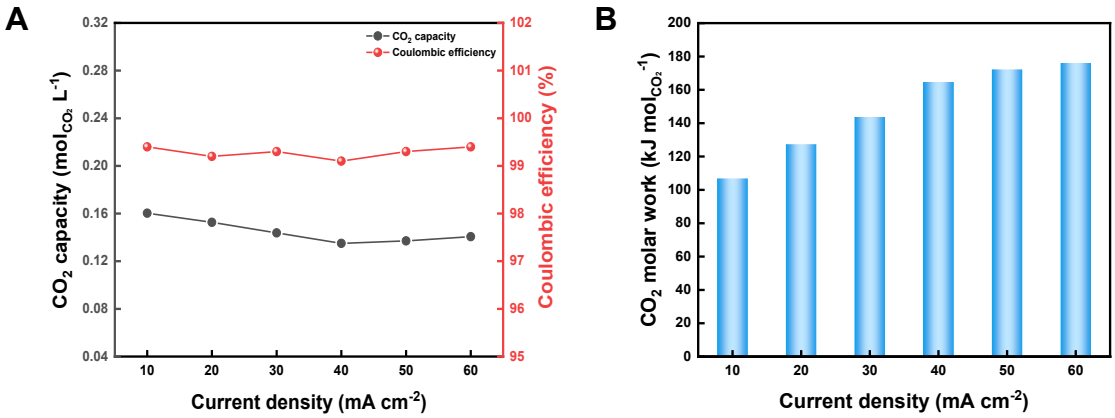

Supplementary Figure 32. (A) CO_2 capacity, coulombic efficiency, (B) CO_2 molar work for each cycle illustrated in the direct air capture cycles reported in Supplementary Figure 31.

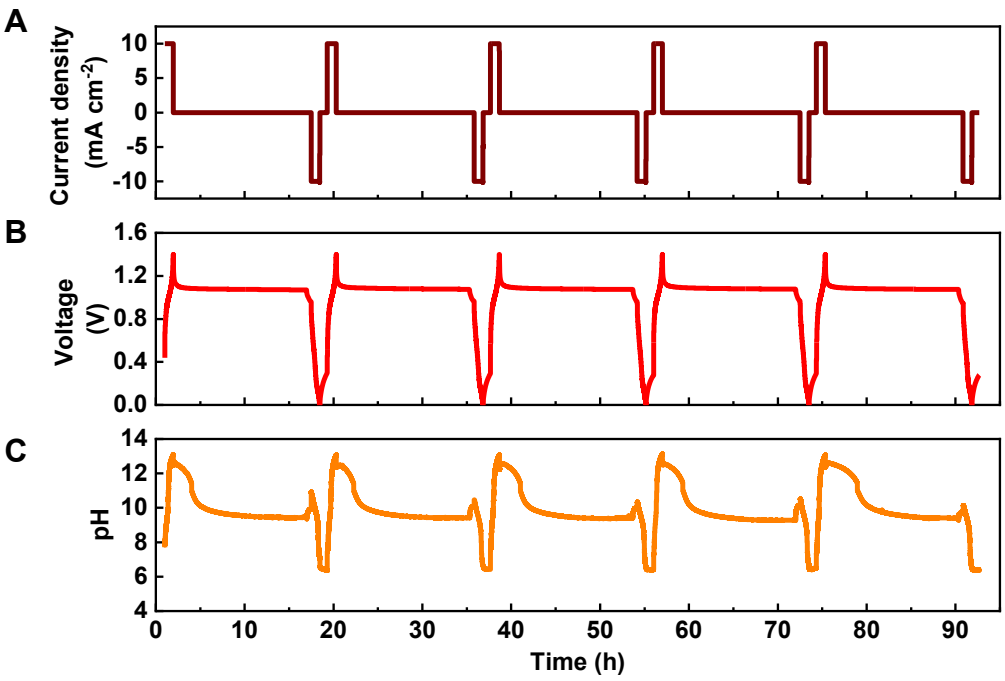

Supplementary Figure 33. Five CO_2 concentrating cycles with CPS-CNT flow cell, which captured CO_2 from air. The cell was cycled galvanostatically at 10 mA cm^{-2} with a voltage cut-off between 1.4 V and 0.0 V and each half cycle ended with a potentiostatic hold until the magnitude of the current density fell below 7.5 mA cm^{-2} (charge) and 5 mA cm^{-2} (discharge). No feed gas was used during the deacidification process. The feed gas was air at 1 L min^{-1} flow rate for the capture step (15 h) and switched to vaccum for the whole acidification and sweep step. After each cycle, residual CO_2 gas in the pipeline was evacuated using a vacuum pump. (A) Current density. (B) Voltage. (C) pH of the negolyte.

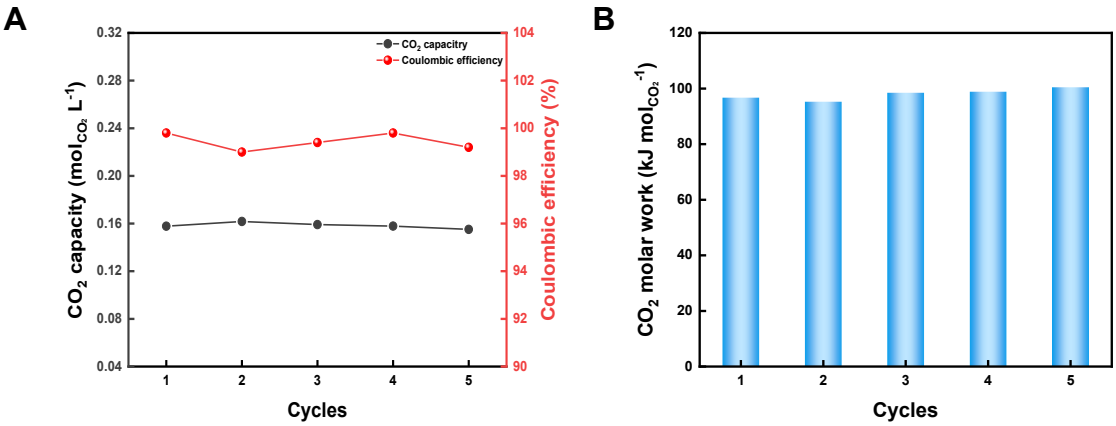

Supplementary Figure 34. (A) CO_2 capacity, coulombic efficiency, (B) CO_2 molar work for each cycle illustrated in the direct air capture cycles reported in Supplementary Figure 33.

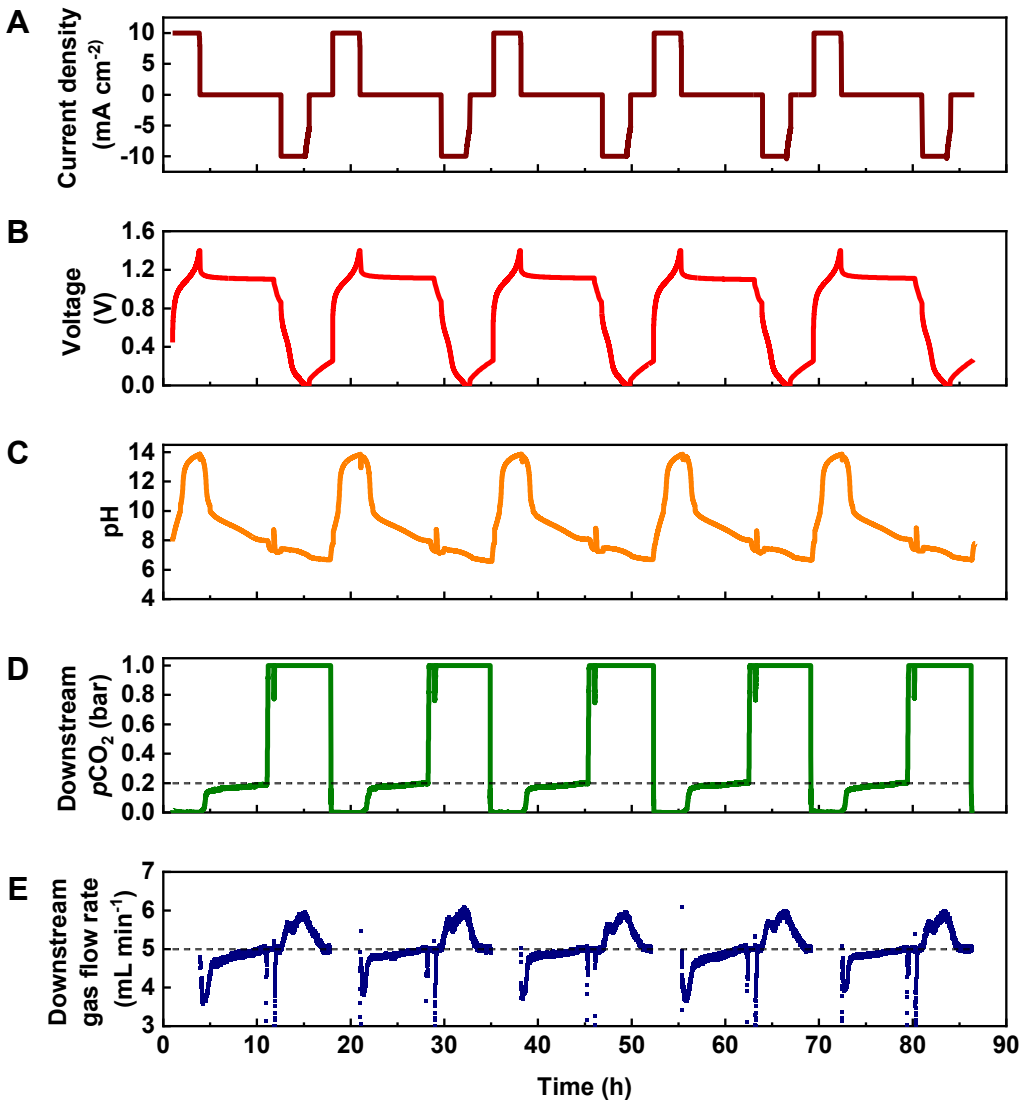

Supplementary Figure 35. Five CO_2 concentrating cycles with H-CPS-CNT flow cell. The cell was cycled galvanostatically at 10 mA cm^{-2} with a voltage cut-off between 1.4 V and 0.0 V and each half cycle ended with a potentiostatic hold until the magnitude of the current density fell below 7.5 mA cm^{-2} (charge) and 5 mA cm^{-2} (discharge). No feed gas was used during the deacidification process. The gas containing 20% CO_2, 20% O_2, and 60% N_2 was fed during the whole capture step, pure CO_2 was fed during the whole acidification and sweep step. After each cycle, residual CO_2 gas in the pipeline was evacuated using a vacuum pump. The initial gas flow rate was set to 5 mL min^{-1}. (A) Current density. (B) Voltage. (C) pH of the negolyte. (D) Downstream CO_2 partial pressure. The black dashed baseline indicates pCO_2 = 0.2 bar. (E) Downstream total gas flow rate. The black dashed baseline is 5 mL min^{-1}.

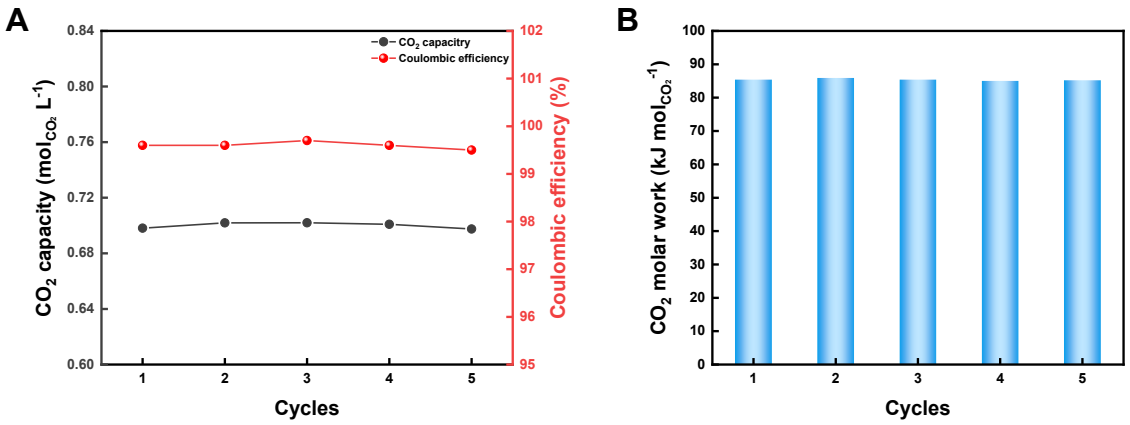

Supplementary Figure 36. (A) CO_2 capacity, coulombic efficiency, (B) CO_2 molar work for each cycle illustrated in the cycles for capture from 20% CO_2, 20% O_2, and 60% N_2 reported in Supplementary Figure 35.

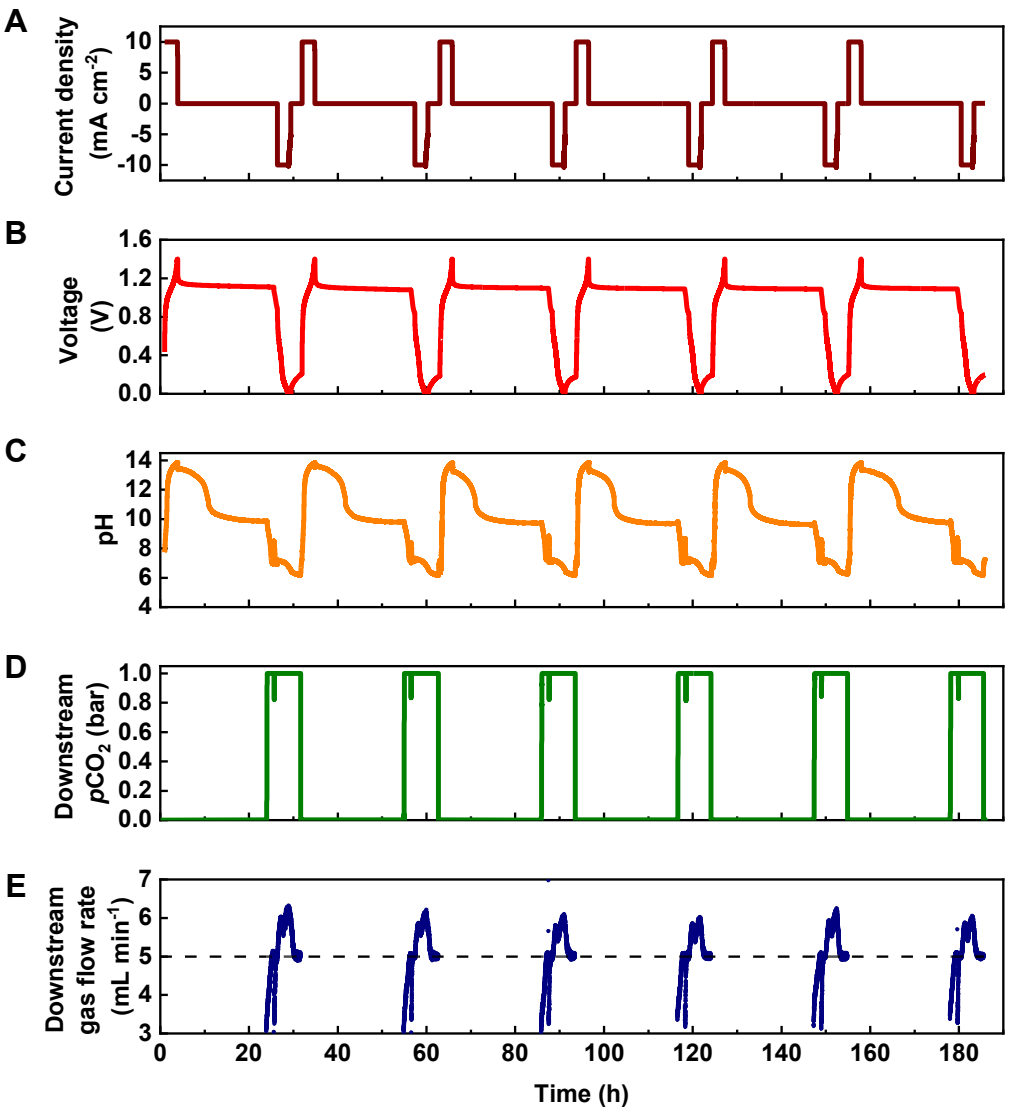

Supplementary Figure 37. Six CO_2 concentrating cycles with H-CPS-CNT flow cell, which captured CO_2 from air. The cell was cycled galvanostatically at 10 mA cm^{-2} with a voltage cut-off between 1.4 V and 0.0 V and each half cycle ended with a potentiostatic hold until the magnitude of the current density fell below 7.5 mA cm^{-2} (charge) and 5 mA cm^{-2} (discharge). No feed gas was used during the deacidification process. The feed gas was air at 1 L min^{-1} flow rate for the capture step (20 h) and switched to pure CO_2 at 5 mL min^{-1} for the whole acidification and sweep step. After each cycle, residual CO_2 gas in the pipeline was evacuated using a vacuum pump. (A) Current density. (B) Voltage. (C) pH of the negolyte. (D) Downstream CO_2 partial pressure. (E) Downstream total gas flow rate. The black dashed baseline is 5 mL min^{-1}.

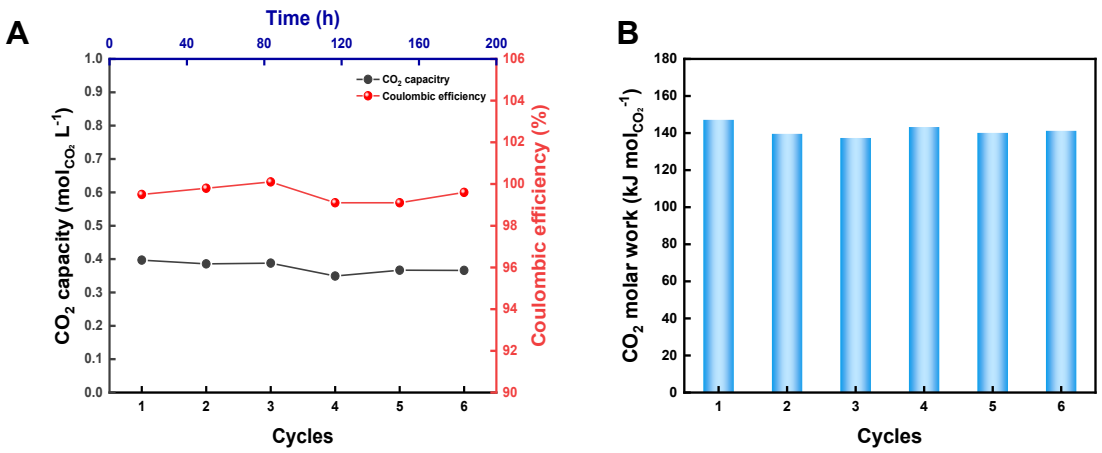

Supplementary Figure 38. (A) CO_2 capacity, coulombic efficiency, (B) CO_2 molar work for each cycle illustrated in the direct air capture cycles reported in Supplementary Figure 37.

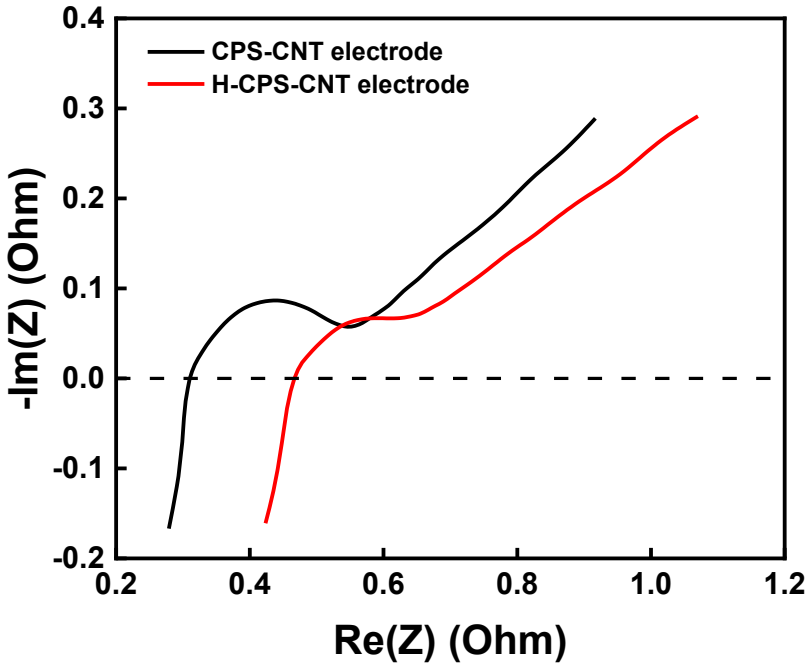

Supplementary Figure 39. Nyquist impedance spectra of CPS-CNT electrode (black line) and H-CPS-CNT electrode (red line) in the hybrid flow cell.

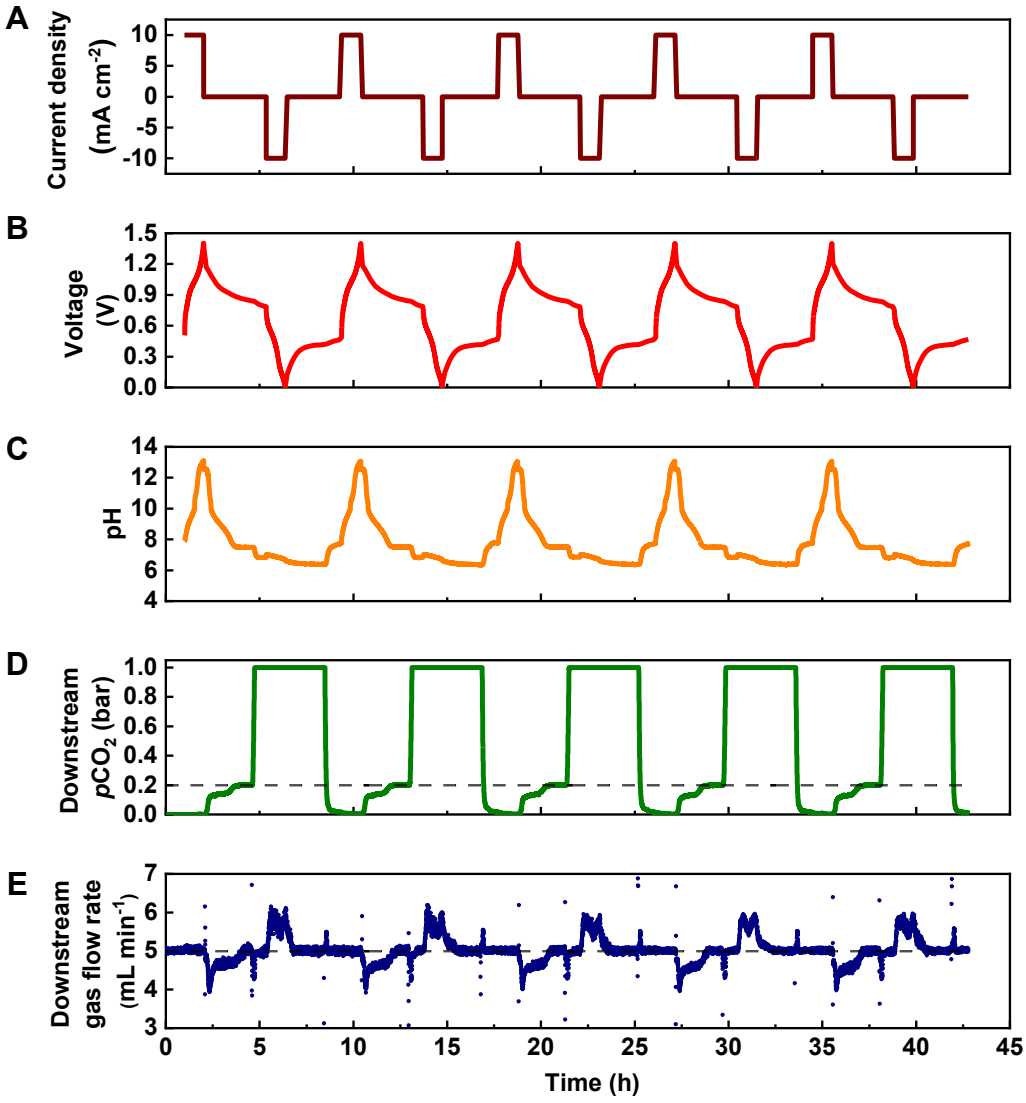

Supplementary Figure 40. Five full CO_2 concentrating cycles with CPS-CNT flow cell. The cell was cycled galvanostatically at 10 mA cm^{-2} with a voltage cut-off between 1.4 V and 0.0 V. The feed gas was pure N_2 during the deacidification process and 20% CO_2 and 80% N_2 for the capture step after deacidification. The feed gas was switched to pure CO_2 during the whole acidification and sweep step. The initial gas flow rate was set to 5 mL min^{-1}. (A) Current density. (B) Voltage. (C) pH of the negolyte. (D) Downstream CO_2 partial pressure. The black dashed baseline indicates pCO_2 = 0.2 bar. (E) Downstream total gas flow rate. The black dashed baseline is 5 mL min^{-1}.

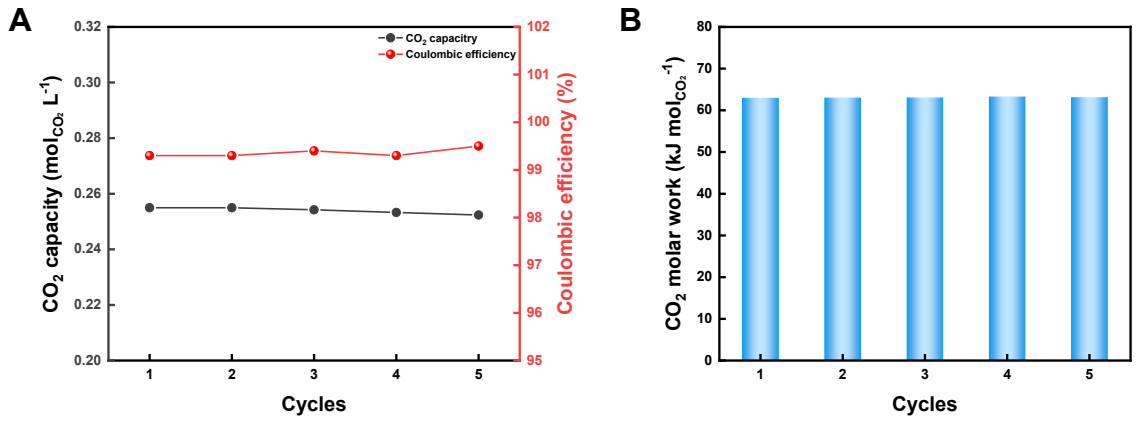

Supplementary Figure 41. (A) CO_2 capacity, coulombic efficiency, (B) CO_2 molar work for each cycle illustrated in the cycles for capture from 20% CO_2 and 80% N_2 reported in Supplementary Figure 40.

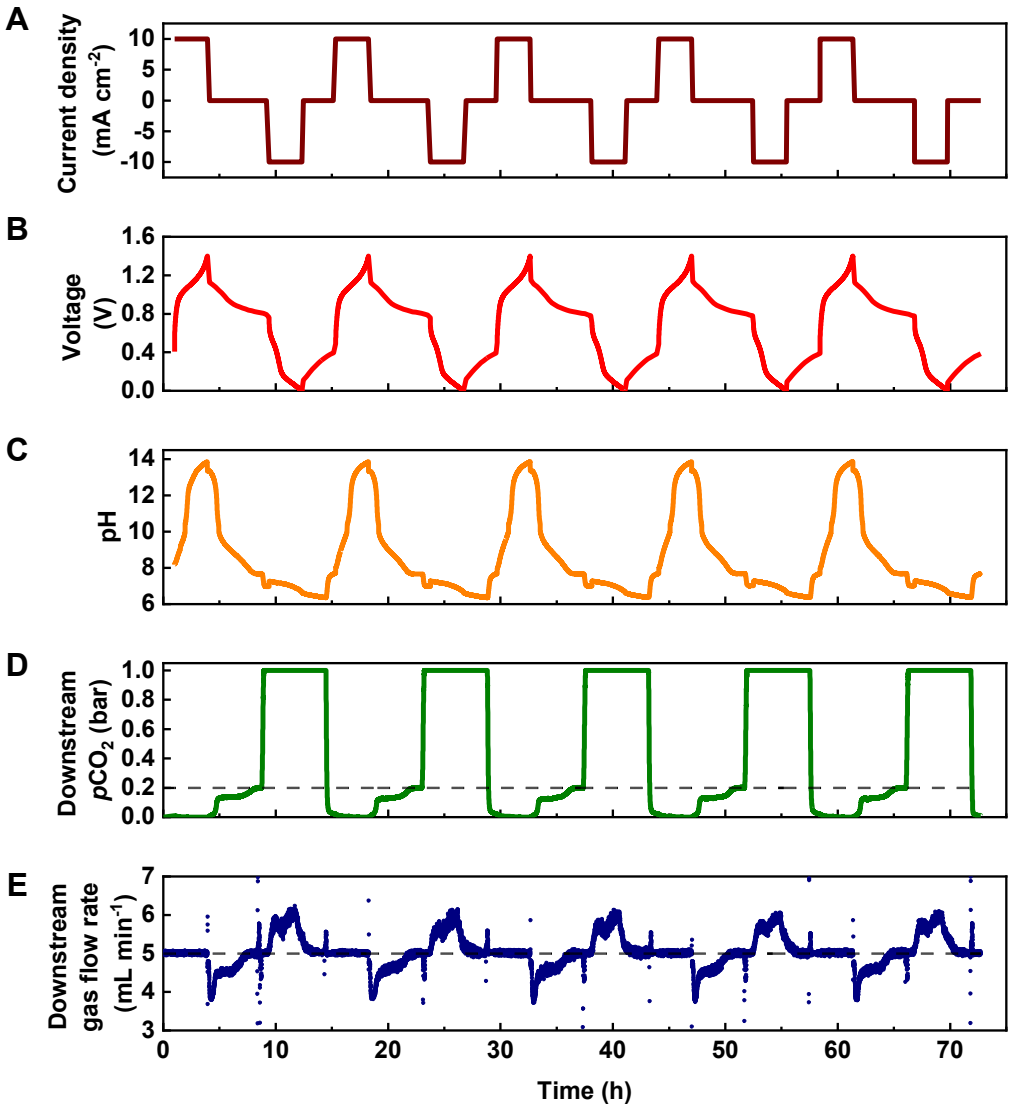

Supplementary Figure 42. Five CO_2 concentrating cycles with H-CPS-CNT flow cell. The cell was cycled galvanostatically at 10 mA cm^{-2} with a voltage cut-off between 1.4 V and 0.0 V. The feed gas was pure N_2 during the deacidification process and 20% CO_2 and 80% N_2 for the capture step after deacidification. The feed gas was switched to pure CO_2 during the whole acidification and sweep step. The initial gas flow rate was set to 5 mL min^{-1}. (A) Current density. (B) Voltage. (C) pH of the negolyte. (D) Downstream CO_2 partial pressure. The black dashed baseline indicates pCO_2 = 0.2 bar. (E) Downstream total gas flow rate. The black dashed baseline is 5 mL min^{-1}.

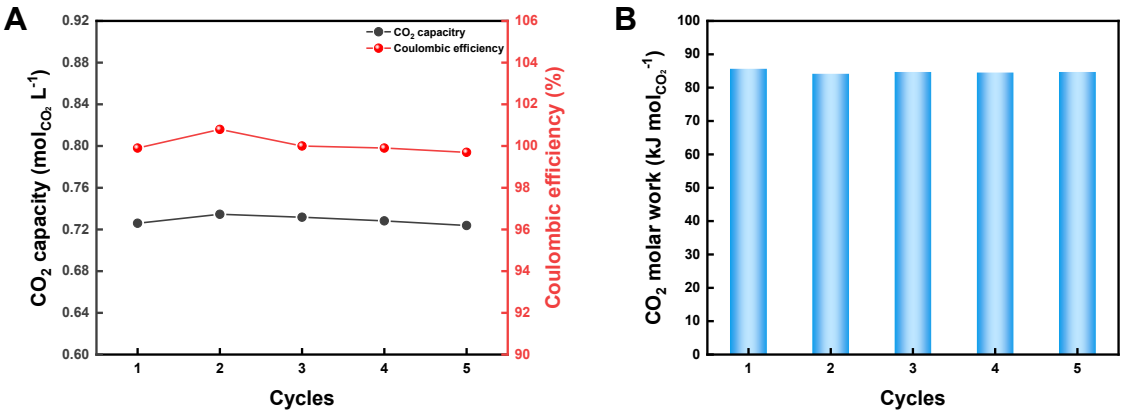

Supplementary Figure 43. (A) CO_2 capacity, coulombic efficiency, (B) CO_2 molar work for each cycle illustrated in the cycles for capture from 20% CO_2 and 80% N_2 reported in Supplementary Figure 42.

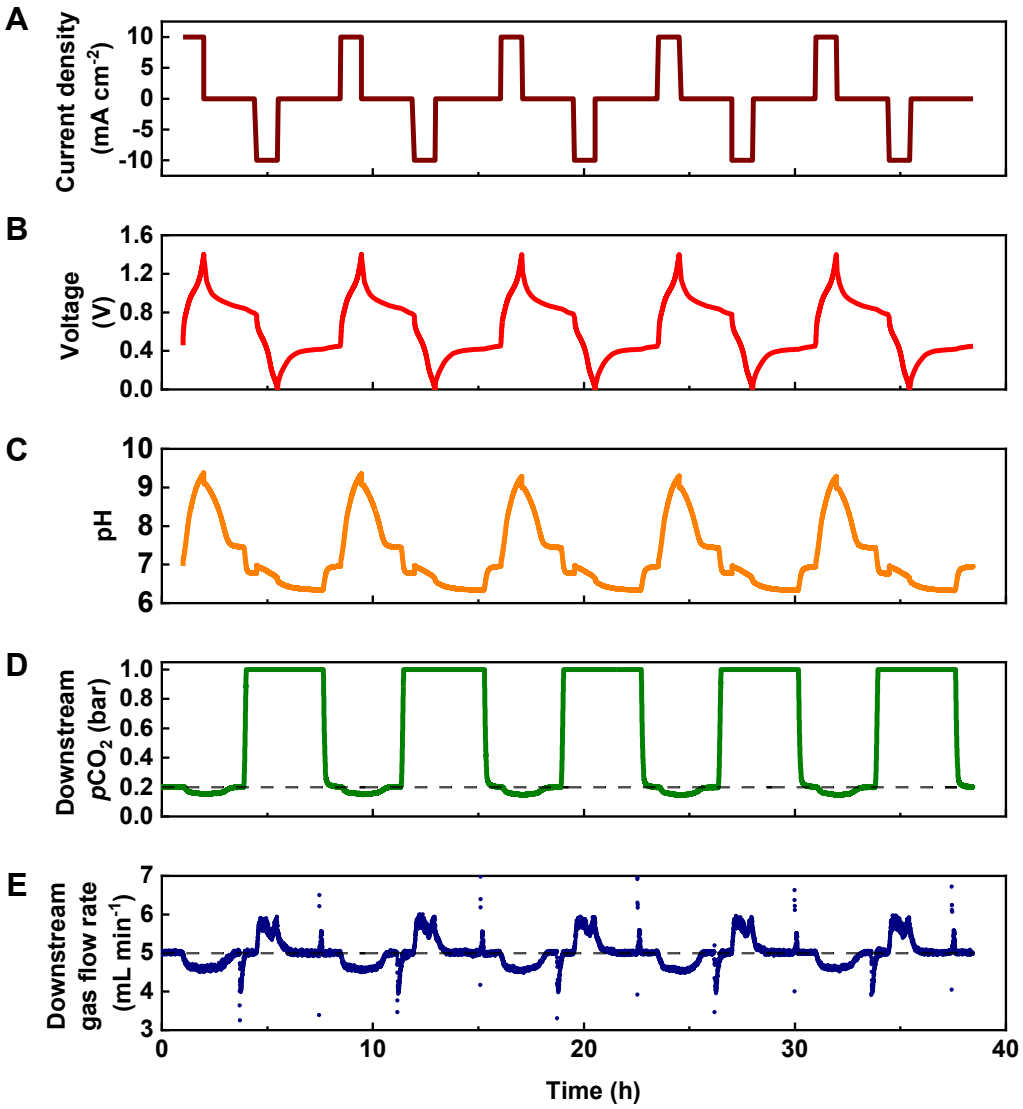

Supplementary Figure 44. Five CO_2 concentrating cycles with CPS-CNT flow cell (4-process cycle). The cell was cycled galvanostatically at 10 mA cm^{-2} with a voltage cut-off between 1.4 V and 0.0 V. The gas containing 20% CO_2 and 80% N_2 was fed during the whole deacidification and capture step, pure CO_2 was fed during the whole acidification and sweep step. The initial gas flow rate was set to 5 mL min^{-1}. (A) Current density. (B) Voltage. (C) pH of the negolyte. (D) Downstream CO_2 partial pressure. The black dashed baseline indicates pCO_2 = 0.2 bar. (E) Downstream total gas flow rate. The black dashed baseline is 5 mL min^{-1}.

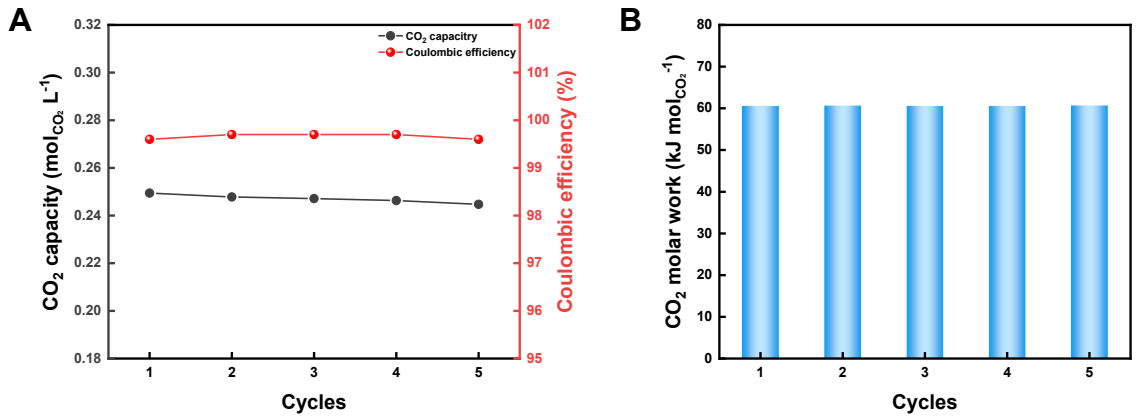

Supplementary Figure 45. (A) CO_2 capacity, coulombic efficiency, (B) CO_2 molar work for each cycle illustrated in the cycles for capture from 20% CO_2 and 80% N_2 reported in Supplementary Figure 44.

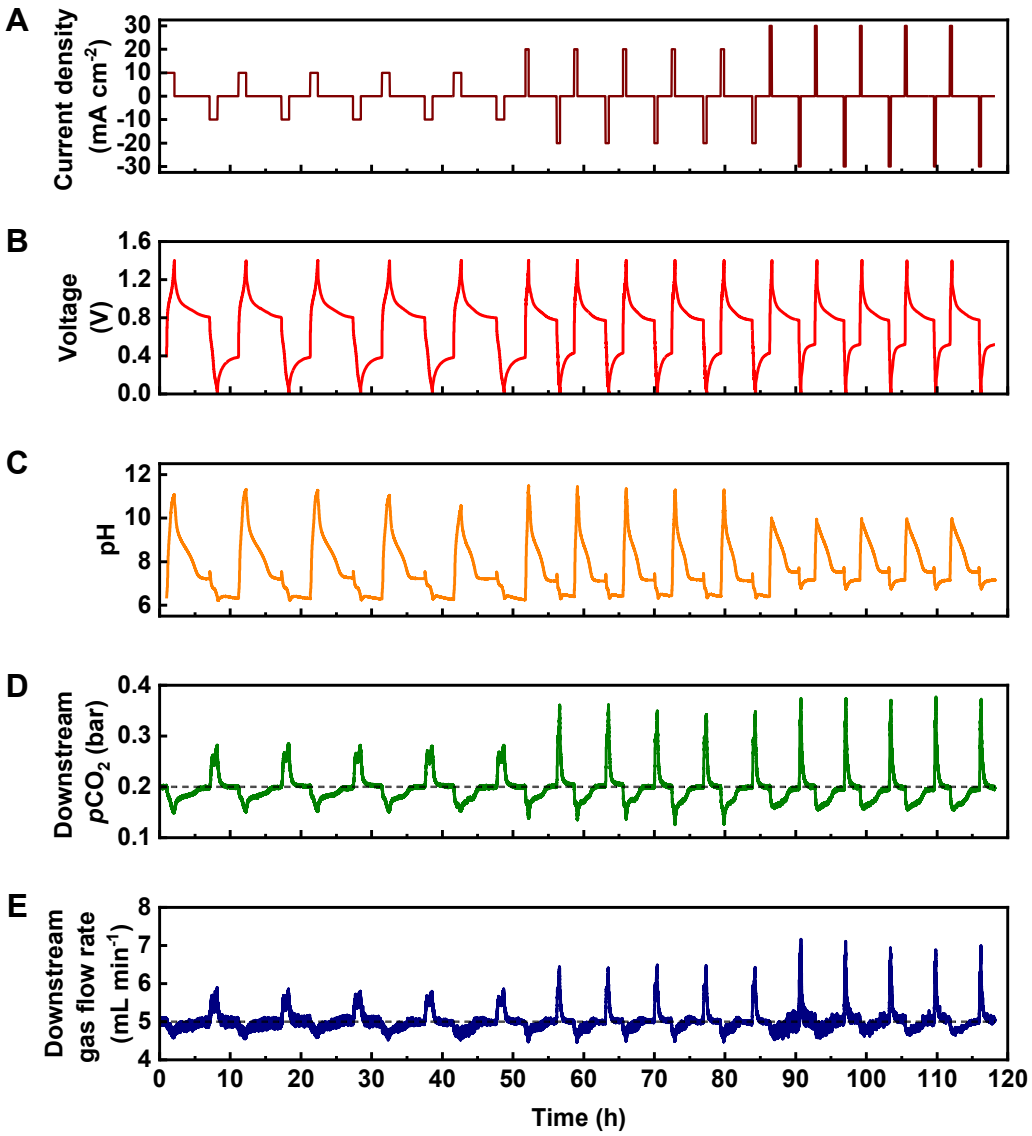

Supplementary Figure 46. Fifteen full CO_2 capture and release cycles with CPS-CNT flow cell at 10 mA cm^{-2} (1^{st} to 5^{th} cycle), 20 mA cm^{-2} (6^{th} to 10^{th} cycle), and 30 mA cm^{-2} (11^{th} to 15^{th} cycle), respectively. The cell was cycled galvanostatically with a voltage cutoff between 1.4 V and 0.0 V. The feed gas was 20% CO_2 and 80% N_2 for the entire step. The initial gas flow rate was set to 5 mL min^{-1}. (A) Current density. (B) Voltage. (C) pH of the negolyte. (D) Downstream CO_2 partial pressure. The black dashed baseline indicates pCO_2 = 0.2 bar. (E) Downstream total gas flow rate. The black dashed baseline is 5 mL min^{-1}.

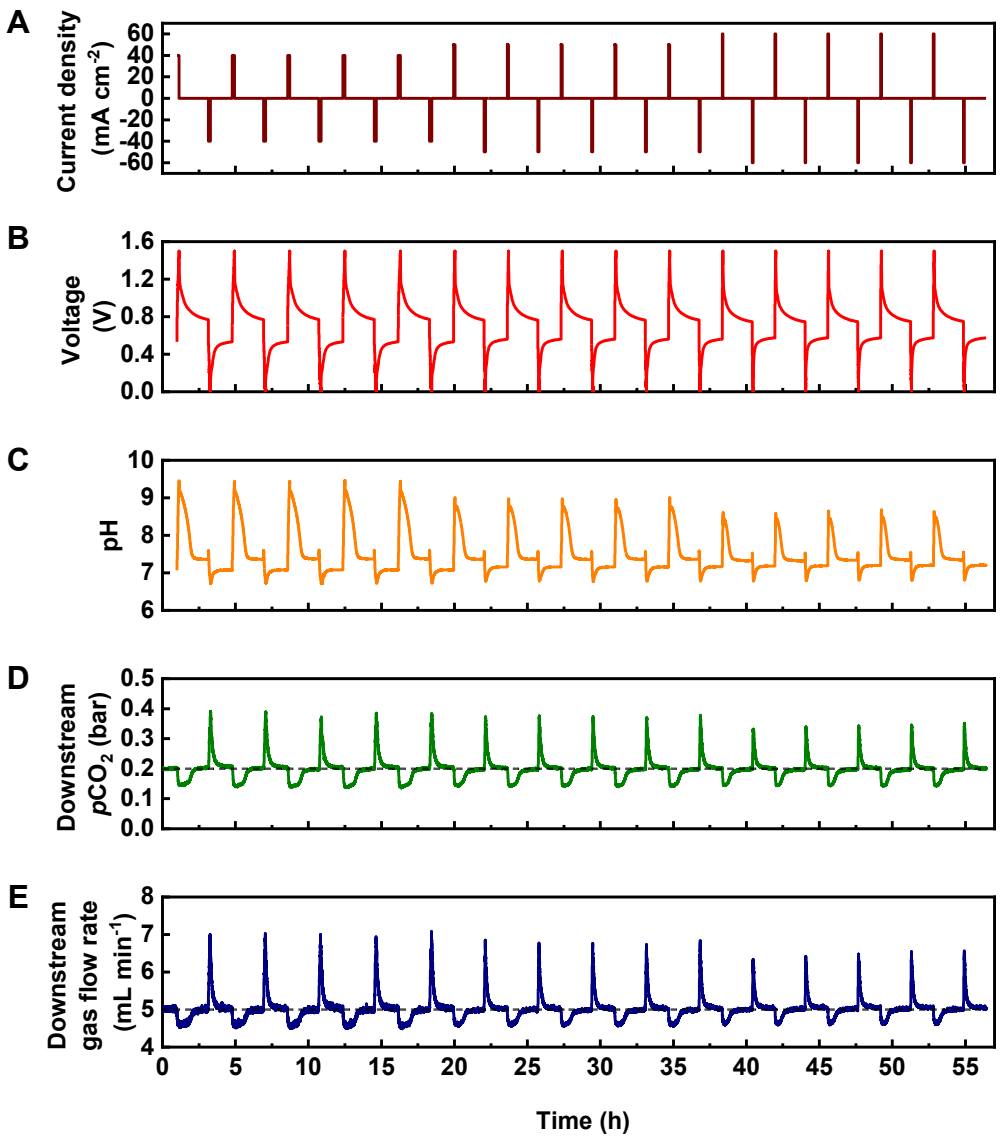

Supplementary Figure 47. Fifteen full CO_2 capture and release cycles with CPS-CNT flow cell at 40 mA cm^{-2} (1st to 5th cycle), 50 mA cm^{-2} (6th to 10th cycle), and 60 mA cm^{-2} (11th to 15th cycle), respectively. The cell was cycled galvanostatically with a voltage cutoff between 1.5 V and 0.0 V. The feed gas was 20% CO_2 and 80% N_2 for the entire step. The initial gas flow rate was set to 5 mL min^{-1}. (A) Current density. (B) Voltage. (C) pH of the negolyte. (D) Downstream CO_2 partial pressure. The black dashed baseline indicates pCO_2 = 0.2 bar. (E) Downstream total gas flow rate. The black dashed baseline is 5 mL min^{-1}.

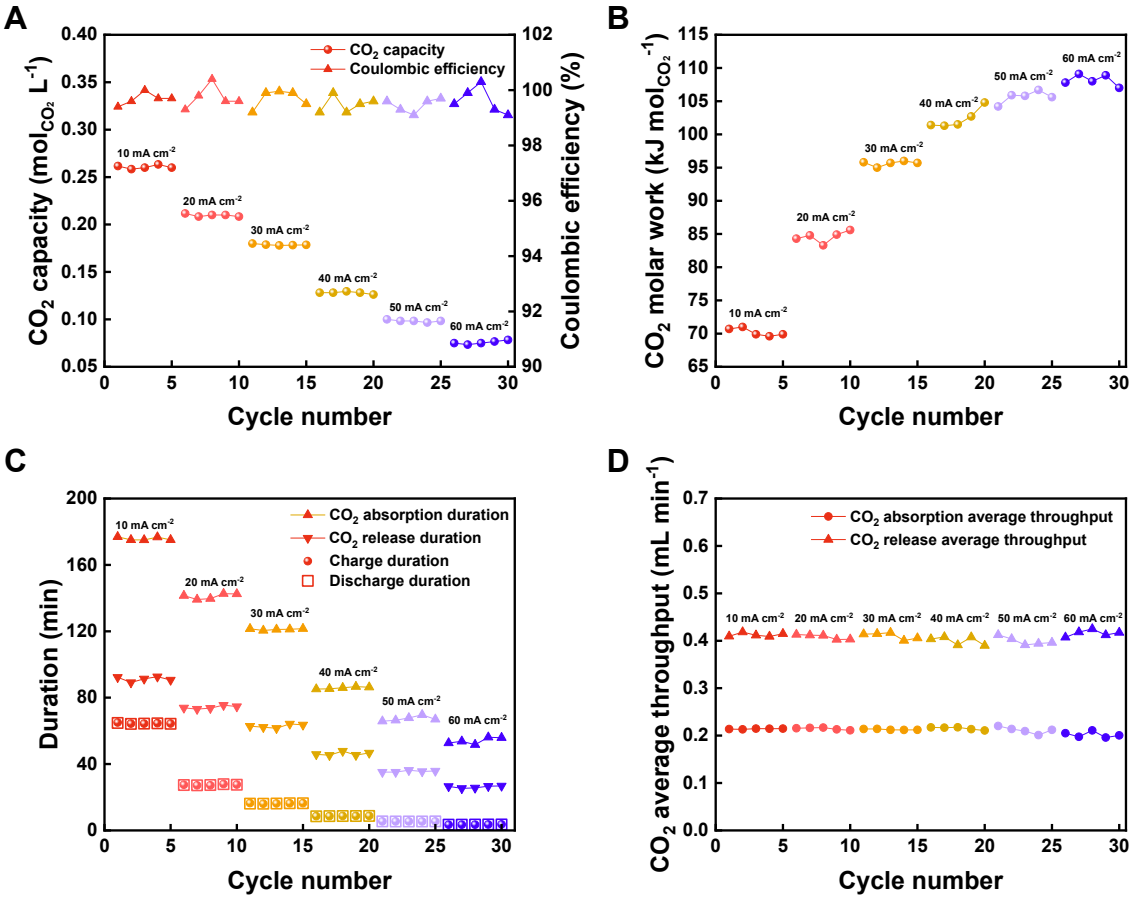

Supplementary Figure 48. (A) CO_2 capacity, coulombic efficiency, (B) CO_2 molar work, (C) Charge and discharge duration, CO_2 absorption and release duration, (D) CO_2 average absorption and release throughput of CPS-CNT flow cell in 1.0 M KCl at different current densities. Five cycles were performed for each current density illustrated in Supplementary Figures 46-47.

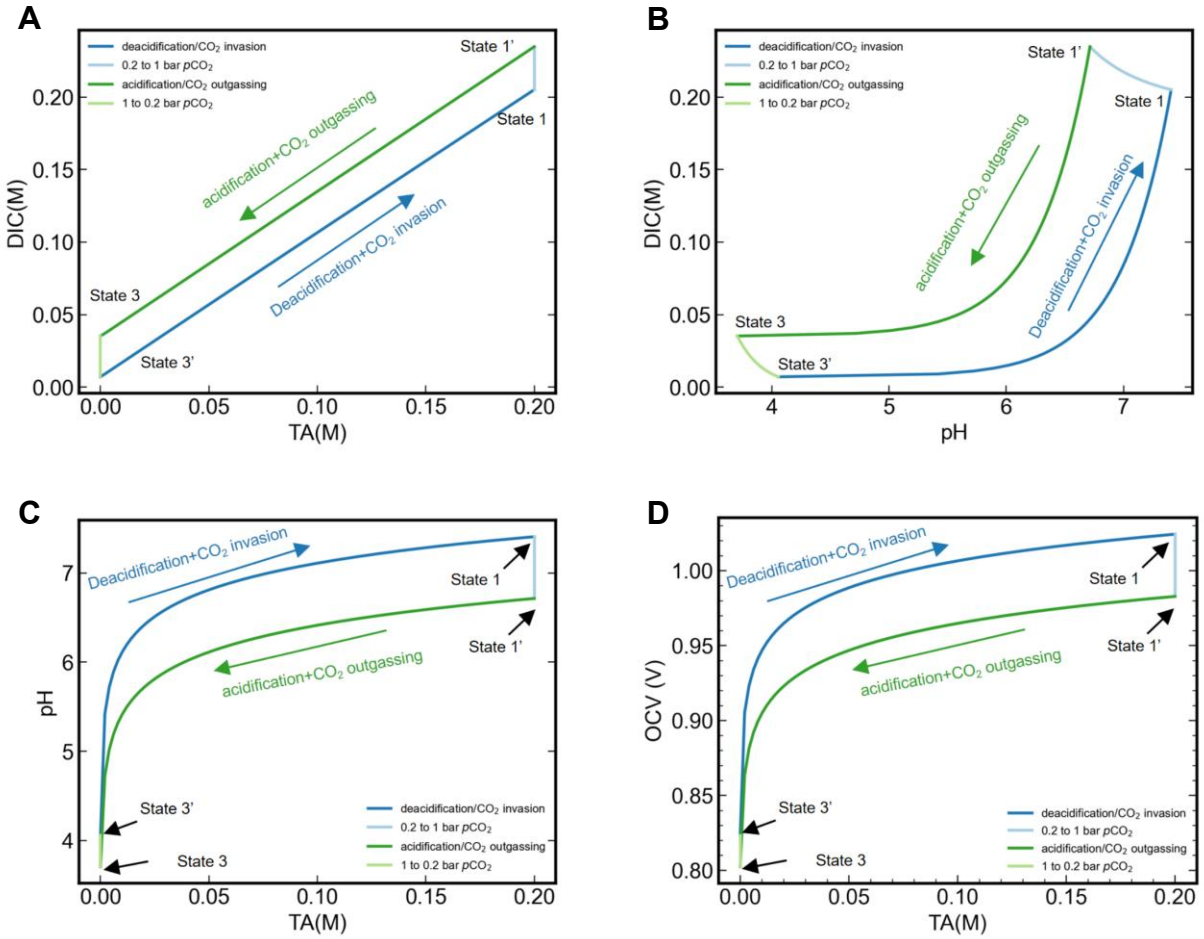

Supplementary Figure 49. Relations among DIC, pH, OCV, and TA in the ideal cycles of a 4-process cycle. Ideal cycle work in kJ can be extracted from panels C. ΔDIC (mol_{CO2}) between states 3 and 1 and be extracted from panels B or measured experimentally. Dividing the ideal cycle work by ΔDIC results in the molar cycle work with unit kJ mol_{CO2}^{-1}.

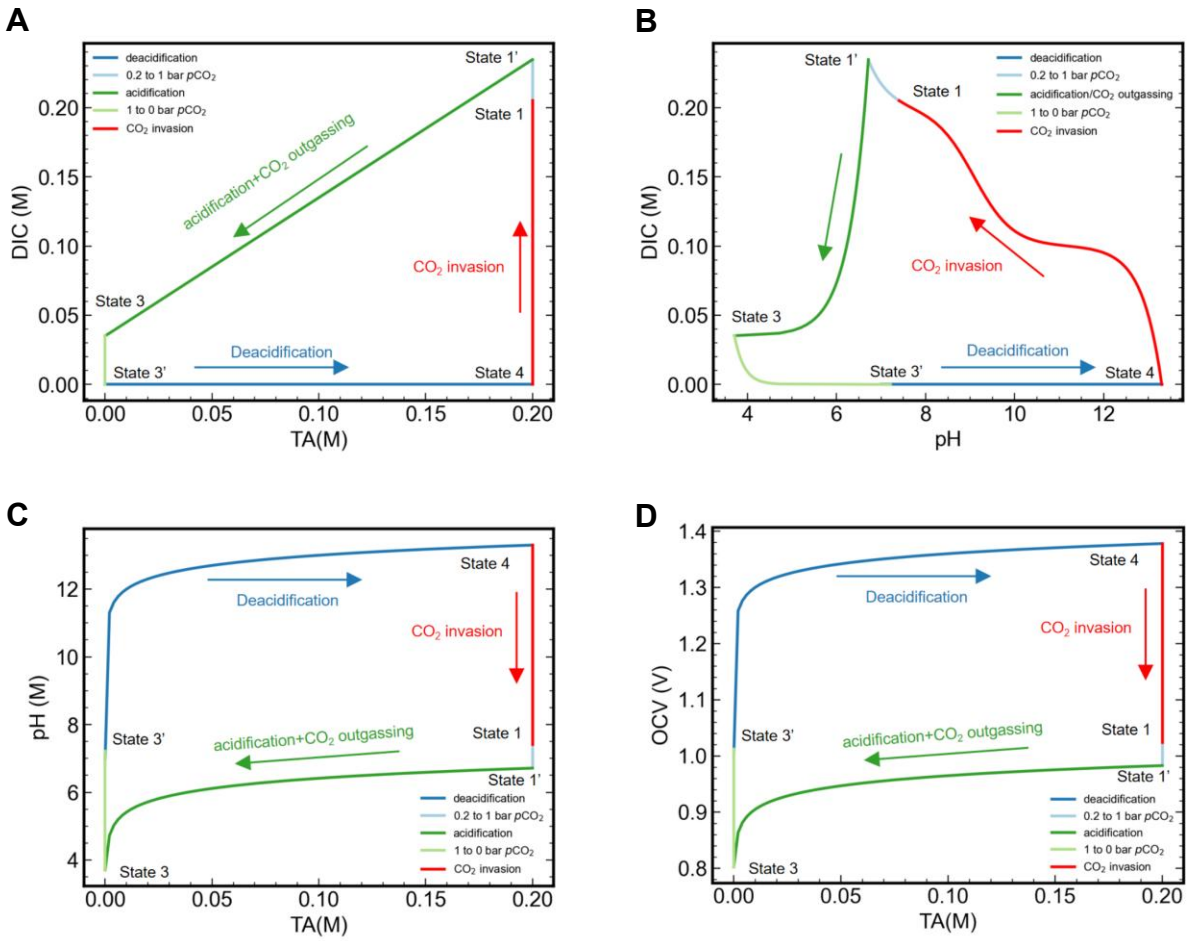

Supplementary Figure 50. Relations among DIC, pH, OCV, and TA in the ideal cycles of a 5-process cycle. Ideal cycle work in kJ can be extracted from panels C. ΔDIC (mol_{CO2}) between states 3 and 1 and be extracted from panels B or measured experimentally. Dividing the ideal cycle work by ΔDIC results in the molar cycle work with unit kJ mol_{CO2}^{-1}.

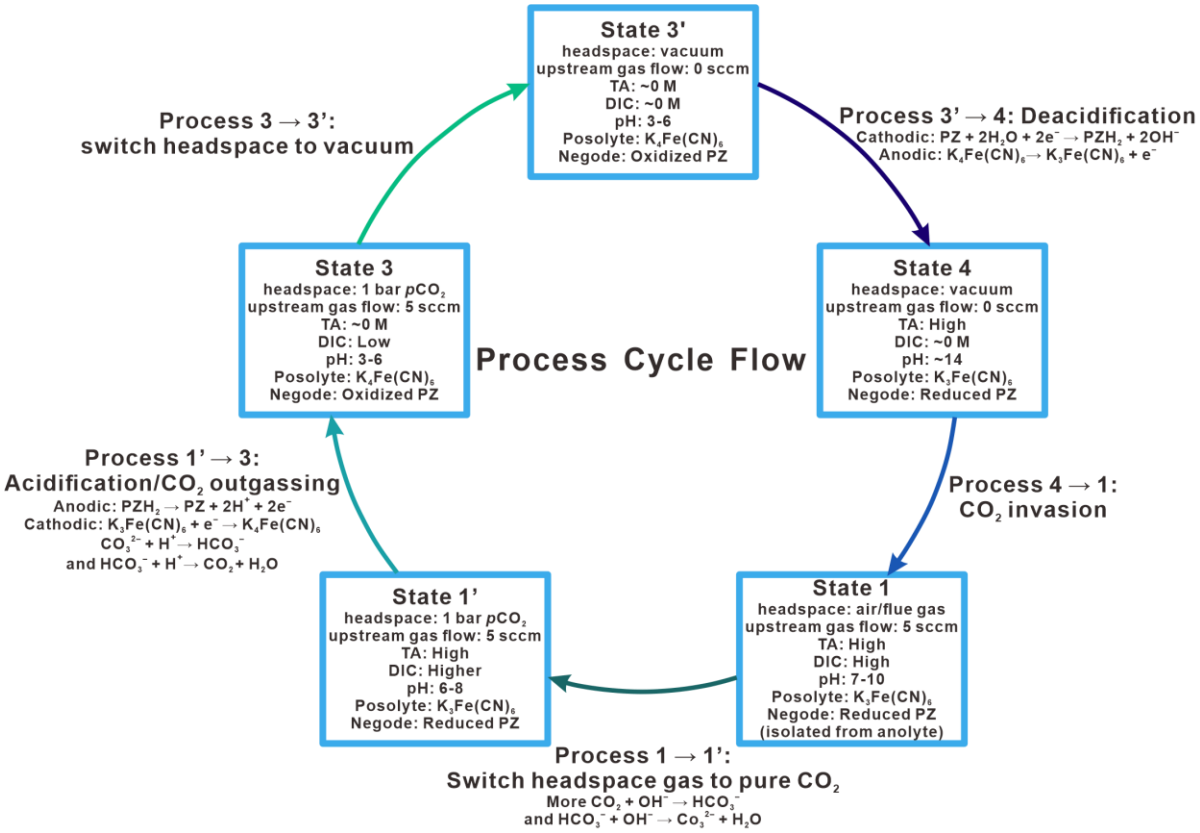

Supplementary Figure 51. Process cycle flow. The solid curved arrows refer to desired reactions in a complete carbon capture/release cycle. Negode is negative electrode. TA is total alkalinity and DIC is dissolved inorganic carbon.

Supplementary Tables

Supplementary Table 1. Summary of the hybrid flow cell performance under varied gas atmosphere conditions

Entry	Figure	Electrode	Feed gas during absorption	Feed gas during release	CO_2 Capacity (mol_{CO2} L^{-1})[a]	CO_2 Capacity (mol_{CO2} L^{-1})[b]	CE (%)	CO_2 molar work (mol_{CO2} L^{-1})[b]	CO_2-to-charge (%)[c]
1	S39	CPS-CNT	20% CO_2 and 80% N_2	100% CO_2	0.230 ± 0.001	0.254 ± 0.001	99.4 ± 0.1	63.2 ± 0.1	90.7 ± 0.1
2	S19	CPS-CNT	20% CO_2, 20% O_2 and 60% N_2	100% CO_2	0.220 ± 0.002	0.226 ± 0.011	98.9 ± 0.1	73.4 ± 3.5	93.2 ± 1.5
3	S22	CPS-CNT	AIR	100% CO_2	0.238 ± 0.001	0.172 ± 0.004	99.4 ± 0.1	104.3 ± 3.8	92.3 ± 0.1
4	S41	H-CPS-CNT	20% CO_2 and 80% N_2	100% CO_2	0.707 ± 0.003	0.759 ± 0.004	100.1 ± 0.4	84.8 ± 0.6	97.3 ± 0.5
5	S34	H-CPS-CNT	20% CO_2, 20% O_2 and 60% N_2	100% CO_2	0.704 ± 0.002	0.700 ± 0.002	99.6 ± 0.1	85.4 ± 0.3	97.2 ± 0.3
6	S36	H-CPS-CNT	AIR	100% CO_2	0.680 ± 0.014	0.375 ± 0.018	99.5 ± 0.4	141.5 ± 3.4	97.1 ± 0.4

[a] The CO_2 capacity was determined by the CO_2 sensor and flow meter, and the detailed calculation method is provided in Eq.(S17). [b] The CO_2 capacity was derived from the measured pH and pCO_2 values according to Eq. (S16) and subsequently used to calculate the molar work of the system. [c] CO_2-to-charge ratio was calculated as the amount of CO_2 (determined by the CO_2 sensor and flow meter) divided by the total applied charge.

Supplementary Table 2. Summary of PCET-based carbon capture systems

Entry	Active materials	Current density (mA cm^{-2})	W_{CO2} (kJ mol_{CO2}^{-1})	CO_2 Capacity (mol_{CO2} L^{-1})	CE (%)	FE (%)
This work	(1) CPS-CNT (2) H-CPS-CNT	10-60	(1.1) 73.4 (20% CO_2, 20% O_2 and 60% N_2) (1.2) 104.3 (Air) (1.3) 176.1 (Air, 60 mA cm^{-2}) (2.1) 85.4 (20% CO_2, 20% O_2 and 60% N_2) (2.2) 141.5 (Air)	(1.1) 0.23 (1.2) 0.17 (1.3) 0.14 (2.1) 0.70 (2.2) 0.38	> 99	> 99
Ref.2	DSPZ	20	61.3 (10% CO_2 and 90% N_2)	~ 0.16	> 99	N.A.
Ref.4	DHPS	10	21.6 (15% CO_2 and 85% N_2)*	N.A.	N.A.	> 95
Ref.5	1,8-ESP	20	(1) 52 (10% CO_2 and 90% N_2) (2) 76 (10% CO_2 and 90% N_2) (3) 70 (20%CO_2, 20% O_2 and 60% N_2)	(1) 0.18 (2) 1.36 (3) N.A.	(1) > 99 (2) > 99 (3) ~ 82	N.A.
Ref.6	Neutral red	< 1	(1) 35 (15% CO_2 and 75% N_2)* (2) 64 (Air) *	(1) ~ 0.11 (2) ~ 0.061	N.A.	N.A.
Ref.7	FMN / $FMNH_2$	10	9.8 (15% CO_2 and 85% N_2)*	~ 0.033.	N.A.	94.3
Ref.8	1-AP nitrate	< 1	(1) 101 (100% CO_2) (2) 162 (Air)*	(1) ~ 0.26 (2) ~ 0.13	N.A.	N.A.
Ref.9	Na_2Q	18	105.6 (12% CO_2 and 88% N_2)*	~ 0.59	N.A.	> 90
Ref.10	1,5-BTMAPAQ	20	65-80 (50% CO_2 and 50% N_2)	~ 0.20	95 ~ 98	N.A.
Ref.11	Cell 1: Bi / AgCl Cell 2: BiOCl / Ag	1	122 (simulated oceanwater ~ 0.07 bar CO_2)	N.A.	N.A.	90.4
Ref.12	MnO_2 / MnOOH	1	33 (15% CO_2 and 85% N_2)	N.A.	N.A.	72 ~ 90

References

1. Pang, S.; Wang, X.; Wang, P.; Ji, Y., Biomimetic Amino Acid Functionalized Phenazine Flow Batteries with Long Lifetime at Near-Neutral pH. *Angew. Chem. Int. Ed.* **2021**, *60* (10), 5289-5298.
2. Jin, S.; Wu, M.; Jing, Y.; Gordon, R. G.; Aziz, M. J., Low energy carbon capture via electrochemically induced pH swing with electrochemical rebalancing. *Nat. Commun.* **2022**, *13* (1), 2140.
3. Roy, R. N.; Roy, L. N.; Vogel, K. M.; Porter-Moore, C.; Pearson, T.; Good, C. E.; Millero, F. J.; Campbell, D. M., The dissociation constants of carbonic acid in seawater at salinities 5 to 45 and temperatures 0 to 45°C. *Mar. Chem.* **1993,** *44* (2), 249-267.
4. Xie, H.; Wu, Y.; Liu, T.; Wang, F.; Chen, B.; Liang, B., Low-Energy-Consumption Electrochemical CO_2 Capture Driven by Biomimetic Phenazine Derivatives Redox Medium. *Appl. Energy* **2020**, *259*, 114119.
5. Pang, S.; Jin, S.; Yang, F.; Alberts, M.; Li, L.; Xi, D.; Gordon, R. G.; Wang, P.; Aziz, M. J.; Ji, Y., A phenazine-based high-capacity and high-stability electrochemical CO_2 capture cell with coupled electricity storage. *Nat. Energy* **2023**, *8* (10), 1126-1136.
6. Seo, H.; Hatton, T. A., Electrochemical direct air capture of CO_2 using neutral red as reversible redox-active material. *Nat. Commun.* **2023**, *14* (1), 313.
7. Xie, H.; Jiang, W.; Liu, T.; Wu, Y.; Wang, Y.; Chen, B.; Niu, D.; Liang, B. Low-Energy Electrochemical Carbon Dioxide Capture Based on a Biological Redox Proton Carrier. *Cell Rep. Phys. Sci.* **2020**, *1* (5).
8. Seo, H.; Rahimi, M.; Hatton, T. A., Electrochemical Carbon Dioxide Capture and Release with a Redox-Active Amine. *J. Am. Chem. Soc.* **2022**, *144* (5), 2164–2170.
9. Huang, C.; Liu, C.; Wu, K.; Yue, H.; Tang, S.; Lu, H.; Liang, B., CO_2 Capture from Flue Gas Using an Electrochemically Reversible Hydroquinone/Quinone Solution. *Energy & Fuels* **2019**, *33* (4), 3380-3389.
10. Jing, Y.; Amini, K.; Xi, D.; Jin, S.; Alfaraidi, A. M.; Kerr, E. F.; Gordon, R. G.; Aziz, M. J. Electrochemically Induced CO_2 Capture Enabled by Aqueous Quinone Flow Chemistry. *ACS Energy Lett.* **2024**, *9* (7), 3526-3535.
11. Kim, S.; Nitzsche, M. P.; Rufer, S. B.; Lake, J. R.; Varanasi, K. K.; Hatton, T. A., Asymmetric chloride-mediated electrochemical process for CO_2 removal from oceanwater. *Energy Environ. Sci.* **2023**, *16* (5), 2030-2044.
12. Rahimi, M.; Catalini, G.; Puccini, M.; Hatton, T. A., Bench-scale demonstration of CO_2 capture with an electrochemically driven proton concentration process. *RSC Adv.* **2020**, *10* (29), 16832-16843.